Teixeira Polez, Roberta; Morits, Maria; Jonkergouw, Christopher; Phiri, Josphat; Valle-Delgado, Juan José; Seppälä, Jukka; Linder, Markus B.; Maloney, Thaddeus; Rojas Gaona, Orlando; Österberg, Monika

Biological activity of multicomponent bio-hydrogels loaded with tragacanth gum

Published in:
International Journal of Biological Macromolecules

DOI:
10.1016/j.ijbiomac.2022.06.153

Published: 31/08/2022

Document Version
Publisher's PDF, also known as Version of record

International Journal of Biological Macromolecules 215 (2022) 691–704

Contents lists available at ScienceDirect

International Journal of Biological Macromolecules

journal homepage: www.elsevier.com/locate/ijbiomac

Biological activity of multicomponent bio-hydrogels loaded with tragacanth gum

Roberta Teixeira Polez [a], Maria Morits [a], Christopher Jonkergouw [a], Josphat Phiri [a], Juan José Valle-Delgado [a], Markus B. Linder [a], Thaddeus Maloney [a], Orlando J. Rojas [a,b], Monika Österberg [a,*]

[a] Department of Bioproducts and Biosystems, School of Chemical Engineering, Aalto University, FI-00076 Aalto, Finland
[b] Bioproducts Institute, Department of Chemical and Biological Engineering, Department of Chemistry and Department of Wood Science, University of British Columbia, 2360 East Mall, Vancouver, British Columbia V6T 1Z4, Canada

ARTICLE INFO

Keywords:
Tragacanth gum
Hydrogels
Cellulose nanofibrils
Lignin nanoparticles
Bioprinting
Tissue engineering

ABSTRACT

Producing hydrogels capable of mimicking the biomechanics of soft tissue remains a challenge. We explore the potential of plant-based hydrogels as polysaccharide tragacanth gum and antioxidant lignin nanoparticles in bioactive multicomponent hydrogels for tissue engineering. These natural components are combined with TEMPO-oxidized cellulose nanofibrils, a material with known shear thinning behavior. Hydrogels presented tragacanth gum (TG) concentration-dependent rheological properties suitable for extrusion 3D printing. TG enhanced the swelling capacity up to 645% and the degradation rate up to 1.3%/day for hydrogels containing 75% of TG. Young's moduli of the hydrogels varied from 5.0 to 11.6 kPa and were comparable to soft tissues like skin and muscle. *In vitro* cell viability assays revealed that the scaffolds were non-toxic and promoted proliferation of hepatocellular carcinoma HepG2 cells. Therefore, the plant-based hydrogels designed in this work have a significant potential for tissue engineering.

1. Introduction

Tissue and organ failures due to disease, injury, and defects have become major health concerns. Organ and tissue donation is a clinical alternative to amend and address such issues. However, due to the shortage of organ donors, there is an increased number of people waiting for transplants [1]. Hence, several solutions to this problem have been implemented, including the use of tissue engineering as a prominent option. The main goal of tissue engineering is to replace or regenerate the normal biological functions of tissues or organs *via* combination of cells and biomimetic matrices. The matrices directly influence tissue formation and regeneration by inducing cell proliferation and migration. They are often designed to closely mimic the natural tissue in the native environment. Not surprisingly, related tissue technologies are being considered in efforts to improve drug screening in preclinical trials, enhancing safety and process speed. In these tissue engineering applications, plant-based materials have gained extensive interest, given that they are non-toxic, biocompatible, and renewable [2,3]. Plant-derived materials are more reproducible compared to biomaterials derived from human or animal origin with lot-to-lot limited reproducibility. In addition, there is a rising concern about biosafety and risk of diseases transmission that can be avoided using plant-based materials. Other advantages of plant-based materials are their mechanical properties, geometrical structure, and porosity in the form of scaffolds [4].

Plant-derived materials, such as tragacanth gum (TG), emerge as promising options for preparing biomaterials in tissue engineering applications. Tragacanth gum is a hydrocolloid of high molecular weight derived from the dry exudate of trunks and branches of different species of *Astragalus*, mostly found in the semi-arid locations and mountains of the Middle East and other regions. TG is an anionic, highly branched polysaccharide that displays string association with cations such as calcium, magnesium, and potassium [5,6]. Acid hydrolysis reveals the presence of neutral and anionic monosaccharides in TG, including D-glucose, L-fucose, L-arabinose, D-xylose, D-galactose, and D-galacturonic acid [7,8]. In traditional local medicine, tragacanth is used as a demulcent for treating digestive complaints and sore throat, and it is also suggested to be analgesic [9]. The viscosity of TG aqueous suspensions and its non-toxic nature support the utilization of TG as a

* Corresponding author.
E-mail address: monika.osterberg@aalto.fi (M. Österberg).

https://doi.org/10.1016/j.ijbiomac.2022.06.153
Received 14 April 2022; Received in revised form 14 June 2022; Accepted 23 June 2022
Available online 28 June 2022

natural stabilizer and thickening agent for food, pharmaceutical, and cosmetic applications [6]. Besides, TG is low cost, widely available, and displays good thermal stability, excellent solubility, and long shelf life [10]. However, until now, the potential biomedical applications of TG have not been fully investigated.

Lignin is another bio-renewable polymer that has attracted interest in recent years for its antimicrobial, antioxidant, and UV-shielding properties, all of which are conferred by the presence of phenolic hydroxyl and methoxy groups in its structure [11–13]. Lignin can be converted into hydrophilic spherical nanoparticles with well-defined surface structures [14,15]. This is an approach that overcomes lignin's structural heterogeneity and low solubility in water and allows further explorations for biomedical utilization [16,17]. Recently, Zhang et al. developed cellulose nanofibril (CNF) -based hydrogel inks for three-dimensional (3D) printing demonstrating that the incorporation of lignin particles to a mixture of alginate and CNF increased the viscosity and provided a better printing resolution, with no negative effect on the proliferation of HepG2 cells on the scaffolds [18]. Lignin has to some extent been used in biomedical research [16], although its application in this field remains relatively unexplored.

Cellulose is another prospective candidate for plant-based materials applied in the biomedical field due to its tunable chemical and physical properties. Cellulose is abundant in nature and mimics the main features of the extracellular matrix (ECM); hence, it has great potential as a low-cost, bio-based material for tissue engineering. When disintegrated, cellulose fibers result in cellulose nanofibrils (CNF) that display a high water-binding capacity and form stable hydrogels due to the hydroxyl groups abundantly available on the CNF surface. Both CNF and TEMPO-oxidized CNF (TOCNF) have been proposed as promising materials for biomedical applications [19–24], and CNF-based products for cell culture have recently been commercialized (*e.g.* GrowDex, CELLINK Bio-ink) [25–27]. However, CNF alone often does not fulfil all requirements when used for tissue engineering and hence addition of other compounds may be needed.

When properly designed, hydrogels have the potential to provide cells with a microenvironment that promotes the regulation of cellular functions, thereby enhancing tissue growth. In this regard, additive manufacturing appears as a versatile technology capable of producing hydrogels with customizable surface structure and tunable mechanical properties. CNF, CLPs and TG all precent interesting properties and we suggest that their combination would be an appealing strategy for plant-based hydrogels with significant potential to improve patients' lives through tissue engineering and regenerative therapies.

Inspired by TG's bioactive properties, TG, TOCNF, and lignin nanoparticles were used to prepare multicomponent hydrogels for 3D printing of biocompatible scaffolds for use in tissue engineering applications. We hypothesize that, by combining the shear-thinning properties of TOCNF with the radical scavenging effect of lignin, and water-binding capacity, and analgesic properties of TG, we could develop biomaterial inks with improved printability and design scaffolds that promote cell proliferation. The combination of these plant-derived materials for tissue engineering has, to the best of our knowledge, not been explored before.

2. Methods

2.1. Materials

Softwood Kraft Lignin powder (SKL, UPM BioPiva™ 100) purified by the LignoBoost process, as reported by the supplier, was used in this study. The kraft lignin was well-characterized in our previous publication [28]. The number and weight average molecular weights (M_n and M_w) of the kraft lignin were 1,193 and 5,250 g mol^{-1}, respectively. The carboxyl groups, aliphatic hydroxyl groups, and total phenolic hydroxyl groups of the kraft lignin were 0.57, 1.89, and 4.05 mmol g^{-1}, respectively [28]. Never-dried birch pulp was used to prepare TOCNF by TEMPO-mediated oxidation (2,2,6,6-tetramethylpiperidine-1-oxyl) at room temperature and pH 10 [29,30]. TOCNF presented a solid content of 1.7 wt% and carboxylic group content of 1.4 mmol g^{-1} as determined in previous reports [31,32]. The average zeta potential was −37 ± 2 mV measured at pH 5. Tragacanth gum (TG) extracted from *Astragalus* species was collected from plants growing in Pakistan (13.6 wt% moisture, 1.9 wt% ashes) and presented viscosity of 3.5 Pa.s (at 10 s^{-1} shear rate and concentration 3 wt%). TG's weight average molecular weight M_w was 475.6 kDa and PDI was 1.25, determined by gel-permeation chromatography (Agilent Infinity 1260 Multidetector GPC) with 0.1 M NaCl as eluent following a method previously reported [33]. The TG sample was dissolved in 0.1 M NaCl at 2 mg mL^{-1} concentration and filtered through the filter with 0.22 μm pores before injection. The monosaccharide composition of TG was determined by acid hydrolysis using high-performance anion-exchange chromatography (HPAE, Dionex ICS 3000) and high-performance liquid chromatography (HPLC, Dionex Ultimate 3000). TG was predominantly composed of galacturonic acid (31.3 wt%), galactose (28.4 wt%), rhamnose (24.2 wt %), and contained small amounts of arabinose (0.3 wt%), glucose (0.1 wt%), mannose (0.1 wt%) and xylose (0.1 wt%). TG was ground and sieved to a powder with mesh size between 150 and 300 μm. The average zeta potential was −33 ± 1 mV measured at pH 5. ABTS (2,2′-Azino-bis (3-ethylbenzothiazoline-6-sulfonic acid)) and sodium persulfate were procured by Sigma-Aldrich. All purchased chemicals and solvents were used without further purification. Hepatocellular carcinoma (HepG2) cells (HB-8065) were obtained from American Type Culture Collection (ATCC, Manassas, VA, USA).

2.2. Lignin particles preparation

Colloidal lignin particles (CLP) preparation followed previously established procedures [34]. SKL powder was dissolved in acetone/water 3:1 (w/w) mixture and stirred for 3 h at room temperature. The lignin solution was filtered using a glass fiber (GF/F Whatman, pore size 0.7 μm) to discard the undissolved aggregates. Then the filtered solution was poured rapidly into water. The resulting CLPs dispersion was placed in dialysis membranes (Spectra/Por dialysis membrane, pore size 6–8 kDa) and dialyzed against water for 3 days to remove acetone and low-molecular-weight impurities. Afterwards, the dispersion was concentrated under reduced pressure at 50°C, followed by filtration using VWR qualitative filter paper (particle retention 12–15 μm). The final concentration of CLPs dispersion was 2.4 wt%. The particle size distribution and zeta potential of CLPs dispersion were measured by a Zetasizer Nano-ZS90 instrument (Malvern Instruments, UK). The average hydrodynamic diameter of CLPs was 106 ± 1.7 nm, PDI was 0.20 ± 0.01 and the average zeta potential was −30 ± 0.2 mV measured at pH 5.

2.3. Hydrogel ink preparation

Aqueous dispersions of TEMPO oxidized cellulose nanofibrils with concentration 1.7 wt% and lignin nanoparticles (CLP 2.4 wt%) were used together with an aqueous solution of tragacanth gum (TG 4.3 wt%) to prepare hydrogel inks. From those dispersions and solutions, five ink formulations were prepared with different ratio of TG to TOCNF (0, 10, 25, 50 and 75 %) (Table 1). Regarding the total composition, the sum of the columns TOCNF (%), TG (%), CLP (%) and water (%) results in 100 %, as described in Table 1. For simplicity, the CLP concentration was kept constant at a level previously found suitable in combination with CNF [18]. The mixing process of the multicomponent hydrogel included vortex mixing at high speed and extrusion using two syringes connected with a female/female Luer lock adaptor under reciprocating movements [18]. This method introduced air bubbles that were removed by centrifuging the syringe (centrifuge 5804, Eppendorf, Hamburg, Germany) for 5 min at 3000 rpm. The hydrogel inks were stored at 4°C until use.

Table 1
Summary of biomaterial ink composition with varied proportions of cellulose nanofibrils and tragacanth gum expressed in dry basis.

Sample codes	TOCNF (wt%)	TG/TOCNF ratio (wt%)	TG (wt%)	CLP/TOCNF ratio (wt%)	CLP (wt%)	Water (wt%)	Total (wt%)
TG00	1.7	0	0.00	5.0	0.085	98.215	100.0
TG10	1.7	10	0.17	5.0	0.085	98.045	100.0
TG25	1.7	25	0.43	5.0	0.085	97.785	100.0
TG50	1.7	50	0.85	5.0	0.085	97.365	100.0
TG75	1.7	75	1.28	5.0	0.085	96.935	100.0

2.4. Hydrogel microstructure and chemical characterization

Atomic Force Microscopy was utilized to analyze the microstructure of the inks. A MultiMode 8 atomic force microscope connected to a Nanoscope V controller (Bruker, Santa Barbara, CA, USA) was used to obtain high-resolution images to check the homogeneity of the hydrogels. Inks were spread on a mica surface and dried at room temperature. The AFM scans (3×3 μm^2) were collected using tapping mode in air with NCHV-A probes (Bruker). The obtained images were analyzed by NanoScope Analysis 1.5 software (Bruker). No image processing was applied. Infrared spectra were recorded between 4000 and 500 cm^{-1} using a PerkinElmer Spectrum Two FTIR spectrometer with ATR. Dry 3D printed scaffolds were used in the measurements.

2.5. Hydrogel rheology

The printability of the hydrogel was assessed through rheological measurements performed for all compositions at 23°C in an Anton Paar MCR302 rheometer (Anton Paar, Germany) using parallel plate geometry (PP25) and a gap size of 1 mm. Shear viscosity data were recorded with a shear rate ranging from 0.01 to 100 s^{-1}. To evaluate the strength of the inks, the linear viscoelastic region (LVR) was identified with a strain sweep ranging from 0.01 to 100 % at a fixed frequency of 10 rad s^{-1}. For the frequency sweep, the frequency range was from 0.01 to 100 rad s^{-1} at a constant strain of 0.5 %.

2.6. Hydrogel porosity

Hydrogel porosity was measured by differential scanning calorimetry thermoporometry (tp-DSC) using a differential scanning calorimeter Mettler Toledo DSC 3+ (Mettler-Toledo Intl. Inc. Instrument, USA) equipped with a cooling system. Hydrogels were placed in 40 μL aluminum pans and hermetically sealed. DSC temperature program and analysis followed previous analytical study [35]. In short, temperature was first brought to −50°C at 20 K min^{-1} to crystalize all the freezable water in the samples. Then it was increased to −0.2°C and held constant until the melting transition was completed. Finally, the temperature was decreased to −50°C at 2 K min^{-1}.

2.7. 3D printing of biomaterial hydrogels

3D printing was carried out in a BIO X bioprinter (CELLINK, Gothenburg, Sweden) with a pneumatic printhead into plastic Petri dishes (100 mm diameter). The printing pattern selected was a grid and the scaffold model was $20 \times 20 \times 5$ mm with infill density of 30 % using a nozzle type of stainless-steel dispensing tip 20G (0.6 mm). Preliminary runs to test 3D printing process conditions were performed to produce scaffolds with good quality and shape fidelity, and parameters were optimized for each ink composition. The printing speed was 10 mm s^{-1}. The dispensing pressure applied in bioprinting for each hydrogel was 30 kPa for TG00, 40 kPa for TG10, 50 kPa for TG25, 80 kPa for TG50, and 130 kPa for TG75.

2.8. Scaffold crosslinking

The scaffolds were crosslinked by ionic crosslinking which is significantly less toxic than organic monomers and can provide ionic linkages with the hydroxyl and carboxylic groups present in TG, TOCNF and CLP. The printed scaffolds were crosslinked by immersion in 5 mL aqueous calcium chloride solution ($CaCl_2$ 1 mol L^{-1}) for 5 min and then washed with deionized water to remove non-crosslinked Ca^{2+} ions. Later the samples were stored in the refrigerator at 4°C prior to further treatments and tests.

2.9. Scaffold swelling behavior

The swelling ability of hydrogels after drying reflects their rewetting and water holding capacity. The hydrogel scaffolds were freeze-dried with a Labconco Freezone 2.5 (Kansas City, MO, USA) for 24 h. The hydrogel scaffolds were frozen at −15°C in a freezer for 12 h, then placed in a lyophilization machine for 24 h and accurately weighed (m_d). The dry scaffolds were soaked in de-ionized (DI) water in a Petri dish at room temperature and weighted after removing the excess of water with a filter paper (m_s), at certain time intervals until it reached equilibrium. The swelling ratio of the hydrogels was determined using the following equation:

$$\text{Swelling}\ (\%) = [(m_s - m_d)/m_d] \times 100 \quad (1)$$

The swelling tests were repeated three times for all samples and the average values were recorded. Moreover, the swelling behavior was evaluated at different pHs (4, 7, and 10).

2.10. Scaffold compression

Mechanical properties of printed scaffolds after crosslinking were measured using a Dynamic Mechanical Analysis equipment Q800 (TA Instruments, New Castle DE, USA) equipped with a 16 N load cell. Scaffolds with 5 mm height were prepared for compression test. Measurements were performed in displacement control mode at a rate of 0.1 N min^{-1} until reaching the final loading of 16 N. Stress−strain curves between 0 and 20 % compressive strain were used to calculate the Young's modulus. Five replicates were performed for each ink composition.

2.11. Scaffold radical scavenging properties

Antioxidant assay was followed as reported by Farooq et al. [12]. ABTS radical cation ($ABTS^{\bullet+}$) was produced by reacting ABTS (2,2′-Azino-bis (3-ethylbenzothiazoline-6-sulfonic acid)) with sodium persulfate. The $ABTS^{\bullet+}$ solution was stored in the dark for 12–16 h before the assay. Freeze-dried scaffolds (10 mg) were mixed with 2 mL of $ABTS^{\bullet+}$ radical solution using a Stuart tube rotator SB2 (Stone, UK) protected from light. After mixing for 1 h, the absorbance at 734 nm wavelength was measured with a UV–vis spectrophotometer (Shimadzu UV-2550) at 25°C. The calibration curve was prepared with aliquots of tannic acid in different concentrations (0.02 to 0.50 mg.mL^{-1}) with 2 mL of $ABTS^{\bullet+}$. Values were reported as tannic acid equivalents (TAE) relative to the dry weight of the sample (mg of TAE g^{-1} of scaffold) and tannic acid equivalents (TAE) relative to the lignin weight (mg of TAE g^{-1} of lignin). All experiments were carried out in triplicates.

2.12. Scaffold degradation

3D printed scaffolds were freeze-dried and weighed (m_0), and then they were incubated in Dulbecco's phosphate-buffered saline (DPBS) at 37°C and 5 % carbon dioxide for 1, 3, 7, 10, and 20 days. After that, the scaffolds were washed with DI water, freeze-dried, and weighed (m_d). The extent of scaffold degradation was determined by the following equation:

$$\text{Degradation } (\%) = [(m_0 - m_d)/m_0] \times 100 \quad (2)$$

2.13. Scaffold cytotoxicity and cell proliferation tests

HepG2 cell line is a valuable tool for screening cytotoxicity of biomaterials. The hepatocellular carcinoma cell line (HepG2) was used as a model cell line in this work due to its high sensitivity to toxins, proving to be a good tool for biocompatibility assessment [18,36]. Moreover, it exhibits epithelial-like morphology, it is reliable and economical substitute for primary or stem cells [37]. HepG2 cells were cultured according to the protocol recommended by the ATCC (HB-8065 American Type Culture Collection). Briefly, cells were cultured onto a 75 cm^2 cell culture flask, for expansion in monolayer, and kept as sub-confluent monolayers in growth medium, Dulbecco's modified Eagle's medium (DMEM, Gibco, 41966029) supplemented with 10 % fetal bovine serum (FBS, Gibco, 10270106). The incubation occurred in a humidifier at 37°C and 5 % CO_2 until cells reached 80–90 % of confluence. Before seeding, cells were detached using TrypLE Express Enzyme (Triple X, Gibco, 12604013) and passaged at a 1:5 ratio into fresh culture flasks. The scaffolds were printed into 12-well plates, crosslinked by immersion in $CaCl_2$ 1 mol L^{-1}, washed with deionized water and incubated overnight in Dulbecco's phosphate-buffered saline (DPBS+, Gibco, 14040133) at 4°C and sterilized under UV light for 25 min in a laminar flow cabinet (KOJAIR Biowizard Silver SL-130 Blue Series) previous to seeding.

One milliliter of HepG2 suspension with a density of 50,000 cells/mL was seeded on scaffolds measuring 15 × 15 × 3 mm. Cell viability and morphology of cells seeded on the scaffolds were observed after 24 h. *In vitro* cytotoxicity and proliferation tests were performed according to the specifications of standard 10993-5 [38] by colorimetric assay using a kit of cell proliferation reagent WST-1 (Roche, Mannheim, Germany, 11644807001) following the supplier's protocol. Briefly, the cells were cultured for 1, 3, and 5 days. Then the scaffolds were washed with DPBS+ and 1 mL of cell medium and 100 μL of WST-1 reagent were added to each scaffold-containing well. After 2 h of incubation, the WST-1 (2-(4-iodophenyl)-3-(4-nitrophenyl)-5-(2,4-disulfophenyl)-2H tetrazolium salt) was oxidized by mitochondrial dehydrogenases to form formazan product. Only viable living cells metabolized WST-1, which led to an increase in formazan dye in the solution that was quantified by colorimetric assay. The assay solution was transferred into a new 96-well plate with a volume of 100 μL for each well, and the optical density (OD) was read at 420 nm using a Synergy H1 multimode microplate reader (Biotek, Bad Friedrichshall, Germany). The background was measured with the same amount of cell medium and WST-1 reagent, and also the control was measured with cells growing in the culture plate with cell medium and WST-1 without the scaffolds. The metabolically active cells reacted with WTS-1 reagent to prepare a soluble formazan dye and the intensity of the color determines the cell viability of scaffolds. All experiments were carried out in duplicate. The cell viability was calculated with the following equation:

$$\text{Viability } (\%) = \left[\left(A_{sample} - A_{background}\right)/\left(A_{control} - A_{background}\right)\right] \times 100 \quad (3)$$

Fluorescence microscopy was used to assess the proliferation of HepG2 cells inside the scaffolds over a 6-day period. A cell-permeable deep-red fluorescent dye, Cell Proliferation Cytopainter (CP, ab176736, Abcam), and a cell-impermeable red fluorescent dye, Propidium Iodide (PI, Molecular Probes, 1159296, Thermo Fisher Scientific), were used to differentiate between dead and living cells. Both phase contrast and fluorescent images were acquired with an Axio Observer Z1 microscope (Carl Zeiss, Jena, Germany), equipped with an iXon Ultra 888 EMCCD camera (Andor Technology, Belfast, United Kingdom) and automated stage. Images were captured with a 10 × 0.3 Ph1 objective, using a 1.6 optovar. Deep-red fluorescent signal from Cell Proliferation Cytopainter was obtained by illumination at 590 nm, an excitation window of 574–601 nm, and emission window of 615–4095 nm (long bandpass filter). Red fluorescent signal from PI was obtained by illumination at 470 nm, an excitation window of 460–488 nm, and collection of emission between 615 and 675 nm. Images were further processed with Zen2 blue and Arivis 3Dxl software package. For 3D reconstructions of acquired images with varying vertical (Z) heights, 5 μm gaps were used.

2.14. Statistical analysis

Values are expressed as mean ± standard deviation (SD). Statistical analysis was performed using analysis of variance (one-way ANOVA) followed by Tuckey test and significance levels were set at $p < 0.05$.

3. Results and discussion

3.1. Effect of TG on TOCNF-CLPs hydrogel rheology

As can be observed in Fig. 1a, the viscosity (η) of TOCNF-CLP hydrogel inks decreased with the shear rate ($\dot{\gamma}$). The addition of TG increased the viscosity of the hydrogels because the solid content increased, but a similar non-Newtonian shear-thinning behavior was observed. This dependence of the viscosity with the shear rate is essential in 3D printing because it is responsible for the shape fidelity after extrusion. During extrusion, at high shear rates, the lower viscosity allows the ink to flow more like a liquid. As soon as the shear rate decreases, the ink viscosity increases immediately, making the print more solid-like [39]. This behavior has been observed for the pure components as well, tragacanth gum [40,41] and cellulose nanofibrils [42,43]. The samples did not present a zero-shear viscosity (ZSV) region, evidencing a weak hydrogel network, showing that the hydrogel physical structure was perturbated without the need of surpassing a shear rate limit [44].

Two distinct regions separated by an inflection point can be observed in the viscosity curves shown in Fig. 1a. In the first region (region I), at low shear rates, the viscosity decreases when the shear rate increases due to the alignment of loosely entangled fibrils towards the flow [45]. In the second region (region II), the strongly entangled fibrils gradually align in the direction of the flow as the shear rate increases. This is observed as a slower decrease in the viscosity as a function of share rate. Similar behavior for CNF has been reported previously [46,47]. As the content of TG in the hydrogel increased, the inflection point separating regions I and II shifted towards higher shear rates (0.68 s^{-1} for TG00 and 2.02 s^{-1} for TG75), which suggests that the gum may adsorb onto TOCNF and function as an interfibril lubricator, facilitating the alignment of the fibrils in the flow direction. Consequently, region I is broader in hydrogels with higher ratios of TG. The effect of increasing the TG content levels off at the highest TG concentrations TG50 and TG75, which showed rather similar viscosity.

The viscosity of TOCNF/CLPs was lower compared to the multicomponent hydrogels that included TG (*e.g.*, 4.2 for TG00 *versus* 5.2, 6.4, 8.5, and 9.6 Pa.s for TG10, TG25, TG50, and TG75, respectively, at 10 s^{-1} shear rate). The increase of the solid content of the hydrogels with the addition of TG caused an improvement in consistency and gelling, leading to an increase in viscosity as the TG amount increases [40,48]. Furthermore, the swelling induced by the electrostatic repulsion between the hydrogel components is expected to be more pronounced as TG is added to the hydrogel, contributing also to the increase in viscosity. It is noteworthy that the ink viscosity should not be excessively

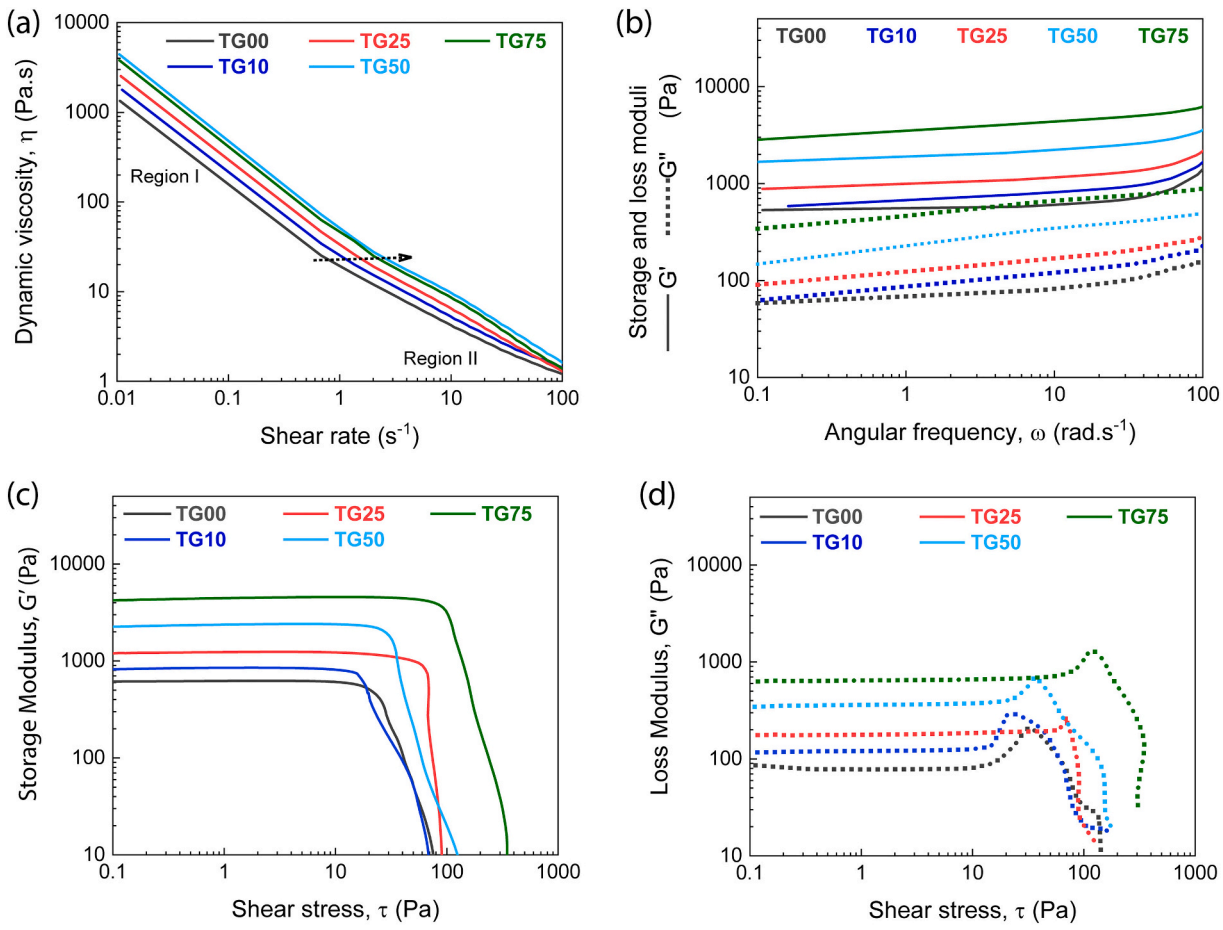

Fig. 1. Rheological properties of the hydrogels. (a) flow curve (dynamic viscosity as a function of shear rate); (b) frequency sweep (storage and loss moduli as function of angular frequency); stress amplitude sweep: (c) storage modulus as a function of shear stress and (d) loss modulus as a function of shear stress.

high for the ink to be able to flow through the nozzle [49].

Fig. 1b shows the oscillatory shear flow at different frequencies. A common behavior was observed for all hydrogel compositions: the storage modulus G′ was higher than the loss module G″, indicating that TOCNF formed viscoelastic hydrogels with a dominant elastic behavior in this frequency range [50,51]. Furthermore, both G′ and G″ increased slightly with the angular frequency, as expected for physically entangled -*via* hydrogen bonding- hydrogels. At low angular frequencies, the cellulose fibrils have more time to orientate in response to the applied stress. As the angular frequency increases, the response time for fibril orientation decreases, resulting in a more elastic behavior of the fibril network as well as more energy dissipation mainly due to interfibrillar friction. Interestingly, the increase in G′ and G″ with the angular frequency is less pronounced as the TG content in the hydrogel increases, which would be in line with enhanced interfibrillar lubrication by TG. Moreover, the values of G′ and G″ increased gradually as the TG concentration was raised. Quantitatively, at 10 rad s^{-1}, the values of G′ and G″ increased from about 599 Pa and 82 Pa to 4352 Pa and 663 Pa when increasing the TG/TOCNF ratio from 0 % to 75 %, respectively. This observation can be explained by the increase in the solid content of the hydrogels after the addition of TG.

The effect of the shear stress on the storage and loss moduli of the hydrogels was evaluated by amplitude sweep tests (Fig. 1c, d). At low shear stress G′ is larger than G″, indicating that the ink is in a stable, solid-like gel state. Above the flow point τ_f (that is, the shear stress where G′ = G″) the hydrogel is in a liquid-like state (G″ > G′) [52]. Except for TG10, the incorporation of TG into the hydrogel increased τ_f considerably (Table 2). The addition of TG also increased the value of G′ and G″ in the linear viscoelastic region (LVR, plateau of the curve at low shear stress) and the yield point τ_y (point where the LVR ends) of the hydrogels, especially for the largest TG concentration tested (Fig. 1c, d and Table 2). In conclusion, TG enhanced the consistency and elastic behavior of the TOCNF-CLPs hydrogels, still allowing their printability when increasing the shear stress or the shear rate.

Table 2
Yield point and flow point of hydrogels.

Samples	Yield point, τ_y (Pa)	Flow point, τ_f (Pa)
TG00	20	31
TG10	15	23
TG25	54	69
TG50	27	38
TG75	100	129

3.2. *Hydrogel porosity*

Fig. 2 shows the porosity of the hydrogels obtained by DSC thermoporometry as a function of TG content. The pore size distribution was in the range of 10 to 120 nm for all the hydrogels, with a peak under 30 nm that decreased as the amount of TG -and consequently the solid content- increased (from 26.3 nm for TG00 to 20.5 nm for TG75, Fig. 2a). As expected, the addition of TG caused a reduction in pore volume and amount of water in the hydrogel due to an increase in the solids content as revealed by DSC thermoporometry. Consequently, stronger interfibril interaction results from the overall reduction in cumulative pore volume as reported previously for pure CNF hydrogels [35] (Fig. S1).

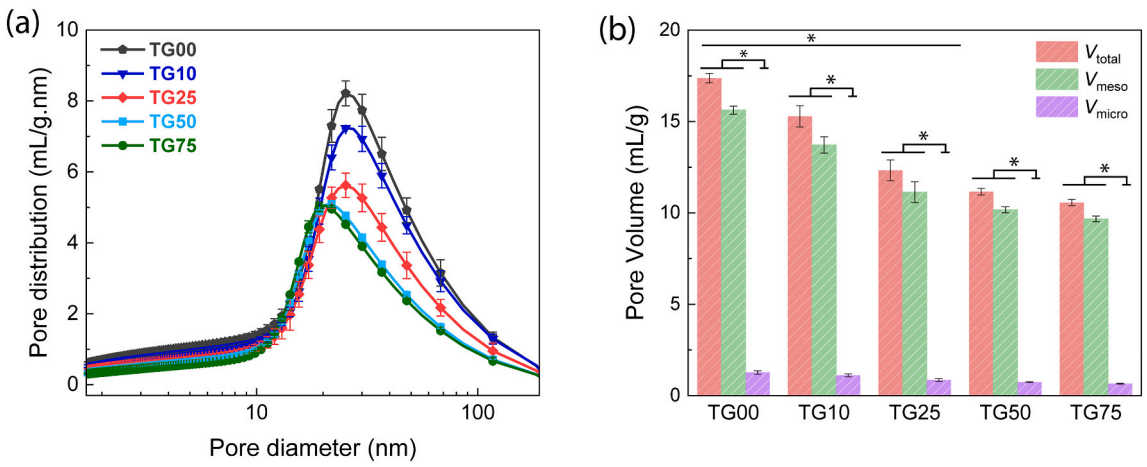

Fig. 2. Results of (a) pore distribution and (b) pore volume of hydrogels based on DSC thermoporometry analysis. *Indicate significant values at the $p < 0.05$.

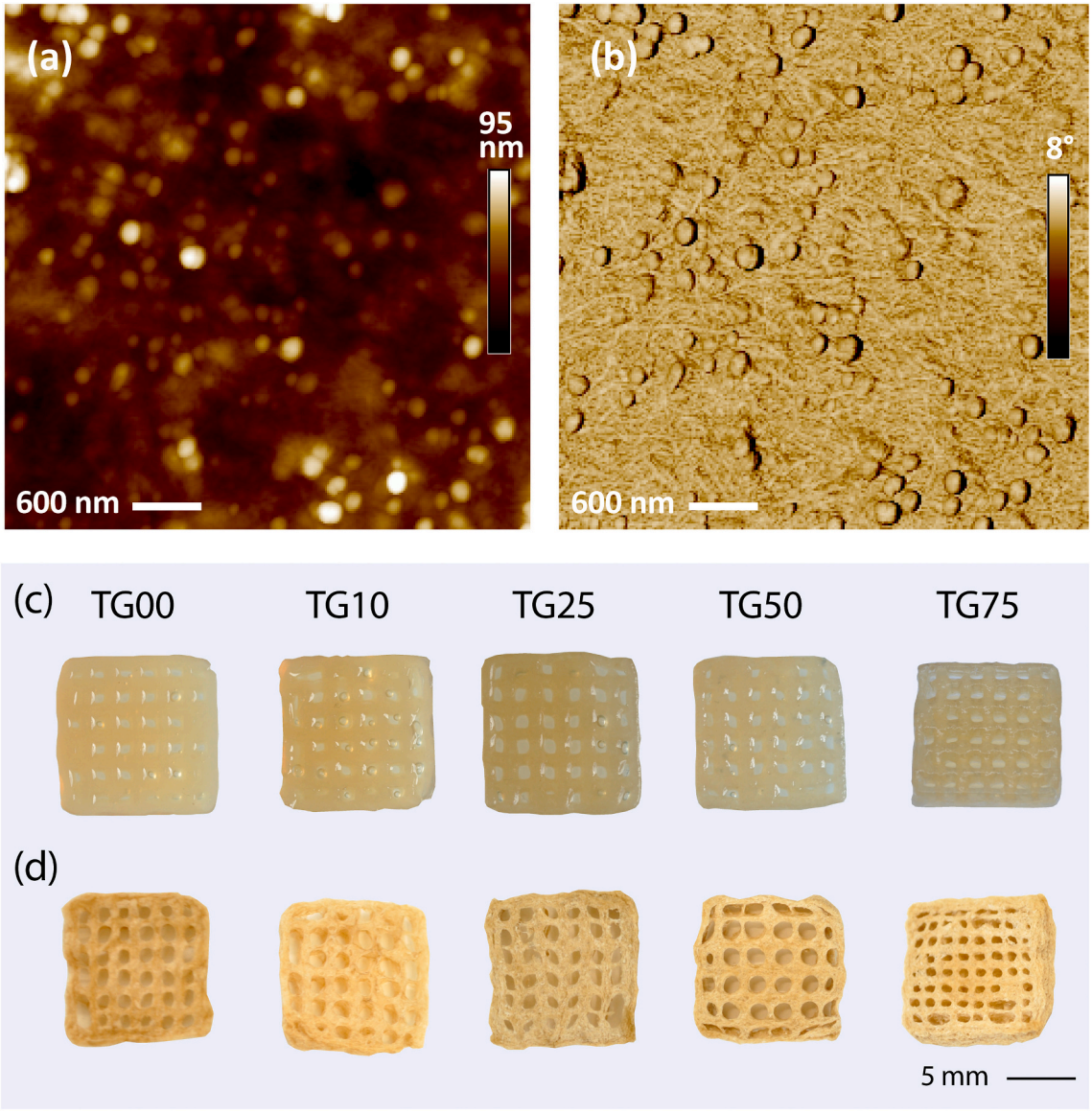

Fig. 3. AFM (a) height and (b) phase images for a film of TG50 sample casted on mica and measured in ambient air. Top view of 3D printed scaffolds with size 20 × 20 × 5 mm of given composition (c) before and (d) after freeze drying.

The hydrogels were mainly composed of mesopores (sizes between 2 and 50 nm) as seen in Fig. 2b, reaching 89.9 % at the lowest gum concentration and 91.5 % at the highest (Table S1). This mesoporous structure suggests high capillarity due to the abundance of small nanopores, which is directly related to the hydrogel diffusion capacity. Regarding this, diffusion influences the liquid transport as well as oxygen and nutrients, and the waste products removal essential for the survival of implanted cells [53]. The total pore volume and mesopore volume diminished from 17.3 to 10.5 mL g^{-1}, and from 15.6 to 9.6 mL g^{-1}, respectively, when gum content incremented from 0 to 75 % TG/TOCNF ratio (TG00 to TG75) (Fig. 2b). Meanwhile, the micropores stayed relatively constant. In hydrogels with greater TG content, the distance between the nanofibers decreased, creating an interconnected 3D network that provided lower porosity. This result clearly indicates that the size of the hydrogel mesopores can be controlled by varying the amount of gum. Pore size and pore network impact other properties, such as mechanical properties and water uptake, as well as cell growth and viability [53].

On a molecular level, CNF and TG interact strongly with bound water in the hydrogel through hydrogen bonds, meaning the bound water does not freeze within the hydrogel and the non-freezing water is believed to represent a one or two molecules thick layer [54,55]. The DSC thermoporometry results suggest that the percentage of bound water increased over the increment of solid content and the free water percentage decreased, as reported previously [35]. As the amount of free water available decreases as the solid content increases, it becomes more confined in smaller pore sizes/volumes, changing its thermodynamic properties [35].

3.3. Hydrogel microstructure and chemical characterization

AFM was utilized to evaluate the microstructure of the hydrogels before 3D printing since ink homogeneity is essential for good printability. Fig. 3a and b shows AFM images of the hydrogel TG50. The structure of the casted films deposited on mica were uniform and did not show phase separation or aggregation of particles or fibrils, indicating colloidal stability and efficient mixing. TG could not be distinguished in the AFM images, but the CLPs were evenly distributed. Similar images (Fig. S2) were observed for the other samples. The hydrogels were also characterized by FTIR. The FTIR spectra (Fig. S3) showed typical bands of polysaccharides and lignocellulosic material.

3.4. Effect of TG on shape fidelity of 3D printed hydrogel scaffolds

Fig. 3c and d shows good printability of scaffolds with grid printing pattern and structure size of 20 × 20 × 5 mm for different ink compositions. The good viscoelastic properties of the inks enabled precise printing of grid structures with a suitable resolution. The printed scaffolds maintained their structure very well, showing no signs of deformation, visible phase segregation, or collapsing after 3D printing. The increase in tragacanth gum content in the hydrogel improved printability and shape fidelity. This is well in line with findings using other types of gums. The incorporation of hydrocolloid guar gum improved both the printability and shape fidelity of chitosan-based inks by increasing the viscosity of the solution [56]. Same trend was observed by Zhu et al. using gellan gum in graphene oxide hydrogels. The increment in gum concentration enhanced the fidelity of filament thickness and fidelity on mesh area [57]. Lignin particles have previously been found to provide improved shape fidelity and printing resolution to CNF alginate scaffolds [18] in line with our results here for TOCNF and TG hydrogels. After freeze-drying, some small deformation in the edges of the scaffold was observed (Fig. 3d). This could be attributed to the slow freezing process, which promoted agglomeration of the TOCNF fibrils and allowed the formation of large disruptive ice crystals [58] damaging the structure of the dried scaffold.

3.5. Scaffold swelling

The swelling behavior of hydrogels depends on their external environment and on how they have been dried. In this study, the swelling ratio was measured as a function of time, pH, and gum content (Fig. 4). The swelling of freeze-dried hydrogels at different soaking times in water is shown in Fig. 4a. Water easily diffused into the hydrogel network during the first 15 min, and after that, the water absorption capacity of all the hydrogels gradually increased with time until reaching a plateau after roughly 1 h. TG enhanced the water uptake ability of the printed scaffolds, with measured swelling ratios of 119 ± 16 % for TG00, 183 ± 41 % for TG10, 288 ± 49 % for TG25, 435 ± 91 % for TG50, and 645 ± 131 % for TG75 after 24 h soaking time. In contrast to the hydrogel's porosity, where the solid content was inversely proportional to the water content, a high solid content resulted in more expansion and adsorbed water within the hydrogel. Similar swelling trend was observed for TG/acrylamide hydrogels reported by Rao et al., where the increase in the amount of TG improved the swelling properties [59]. The high water absorption of all hydrogels can be attributed to the hydrophilic groups present in the chemical structure of all hydrogel components. The electrostatic repulsion between the hydrogel components also favors the swelling of the scaffold, increasing the amount of water entrapped inside [60,61]. Probably both the CLPs and TG decreased the irreversible association of the fibrils during drying, that is frequently observed for CNF hydrogels, consequently promoting efficient rewetting [62,63]. The enhanced reswelling at higher TG content may also be a result of the higher degree of bound water in the hydrogel. Greater swelling ratio indicates better ability of the scaffolds to exchange nutrients when used in 3D cell cultures. It also provides porous structures beneficial to cell migration [64,65].

Swelling of the hydrogel scaffolds was influenced by the pH of the medium as observed in Fig. 4b. When pH increased from 4 to 10, the swelling ratio increased clearly. Hydroxyl and carboxyl groups are the main functional groups of TOCNF, CLPs, and TG contributing to the rehydration of the hydrogels [66–68]. The deprotonation of carboxyl groups as the pH increased enhanced the swelling of the hydrogels due to electrostatic repulsion between the hydrogel components [60,61]. These results are in agreement with previous work by Kiani et al., who observed that the swelling capacity of TG-based hydrogels were dependent on the pH and ionic strength [69]. Another reason could be that the freeze-drying process affects the interfibrillar network of the fibrillar material. Therefore, the shrinkage decreases with the increase of TG. Adding the water-soluble TG probably enables more reversible water uptake.

We note that the variability in swelling results was high. Statistical analysis confirms that there is a statistically significant difference between TG75 and TG50 but not between TG00, TG10 and TG25 or between TG50 and TG75. Similarly, while the increase in swelling when going from pH 4 to pH 10 is clear, the behavior in water is less obvious. There appears to be a decrease in swelling between pH 4 and water for some of the samples. However, this change is not statistically significant.

3.6. Scaffold compressive strength

Unconfined compression assays were performed to evaluate the stiffness of the hydrogels. Scaffold elasticity (as well as geometry and composition) induces different stimuli for tissue formation and differentiation, hence the hydrogel should have equivalent mechanical properties as the native tissue in the intended application [70]. The combination of biomechanical signals and interactions between cells and the extracellular matrix directs the cell phenotype [71,72]. Moreover, the cells cultured on stiffer substrates proliferate faster and migrate slower compared to those cultured on soft substrates [73].

The stress-strain curves of the scaffolds showed a nonlinear elastic behavior without any sign of fracture up to 70 % strain (Fig. 5a). The deformations during compression due to water loss was pronounced in

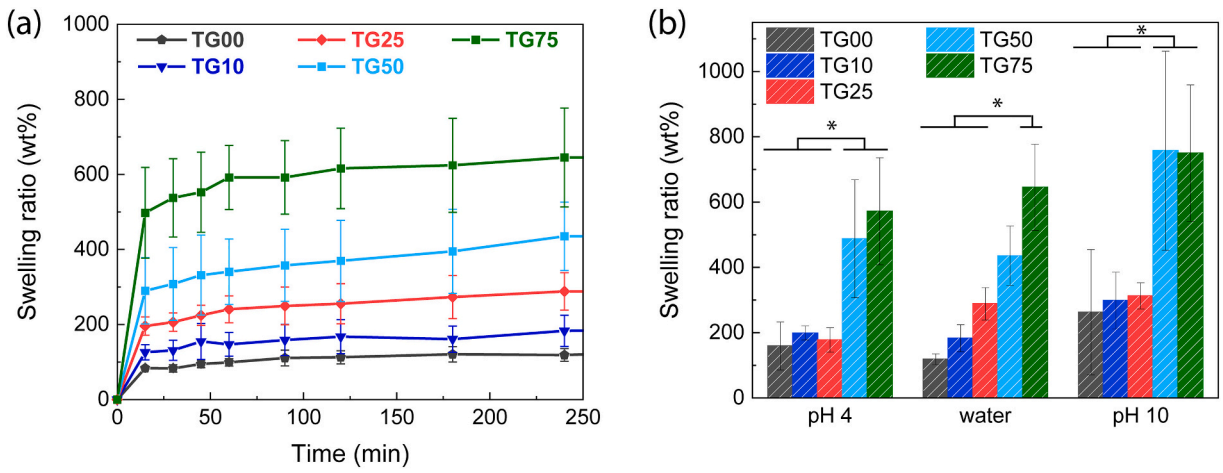

Fig. 4. Swelling behavior of dried scaffolds (a) in DI water as function of time and (b) as function of pH after 240 min. Results expressed as mean ± SD, n = 3. *Compares brackets indicating significant values at the $p < 0.05$.

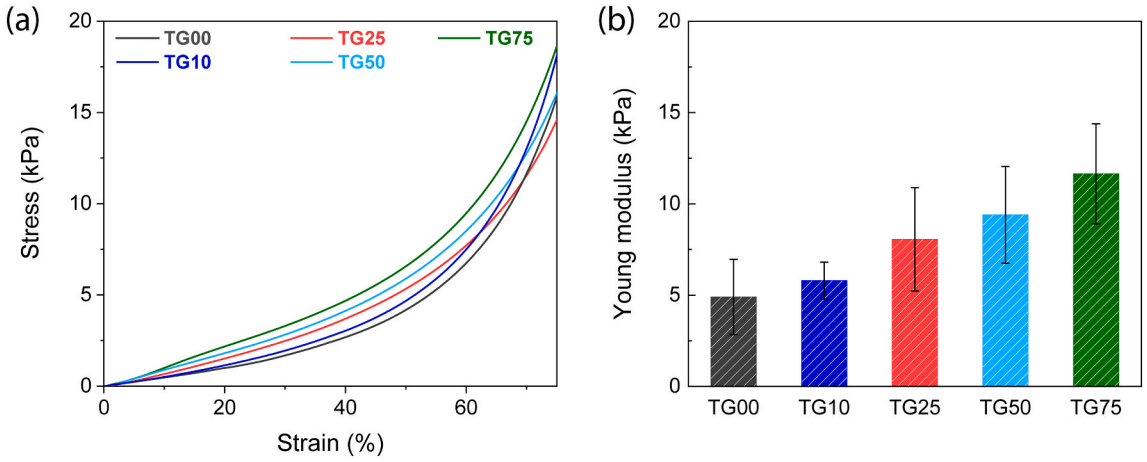

Fig. 5. (a) Stress-strain curves from compression assays for all hydrogel scaffolds. (b) Young's compressive moduli of hydrogel scaffolds. Results expressed as mean ± SD, n = 5.

scaffolds with lower solid content because of higher water content and porosity. The curves can be divided into two regions. In the first region, a linear deformation at low strain values is observed. In the second region, there is a pronounced increase in stress due to densification of the scaffolds resulted from diminishment of porosity and water release [74,75]. Compressive moduli were calculated from the linear region of the curves up to 20 % strain for all compositions. TG increased the Young's modulus of the hydrogels in a concentration-dependent manner (Fig. 5b). The Young's moduli of the hydrogels varied from 5.0 to 11.6 kPa, and thus they can be classified as soft gels with stiffness in the range of skin, muscle, liver, and brain tissues [76–80]. An advantage of our results is that the stiffness can be varied by varying the TG content to optimize the hydrogel for application. For comparison, values between 1.30 ± 0.21 kPa and 1.50 ± 0.14 kPa have been previously reported for the Young's moduli of CNF-CLPs hydrogel [18]. The Young's moduli of our TOCNF-CLPs-TG hydrogel scaffolds were comparable to other hydrogel polymers used in tissue engineering: 15.8 ± 2.0 kPa for alginate, 7.5 ± 1.0 kPa for gelatin methacrylamide (GelMA) crosslinked with 25 mM ammonium persulfate/tetramethylethylenediamide (APS/TEMED) [81], and 14.1 ± 1.9 kPa for poly(ε-caprolactone) (PCL) scaffolds [82].

3.7. Scaffold radical scavenging effects

Reactive oxygen species (ROS) such as hydroxyl radicals (•OH), superoxide ($O_2^{\bar{}}$•), and hydrogen peroxide (H_2O_2) are generally produced during implantation of biomaterials for tissue engineering therapy. Excessive ROS can cause apoptosis and inflammatory signaling leading to incomplete recovery of damaged tissue [83,84]. In this regard, the control of oxidative stress generated during biomaterial transplantation is essential and several studies have confirmed that tissue regeneration improves when antioxidants are used [85,86]. Lignin has radical scavenging properties and was used as antioxidant in the hydrogel composition. Its antioxidant activity is due to the presence of phenocarboxylic acids in its structure (p-coumaric acid, ferulic acid, p-hydroxybenzoic acid) [87]. Some authors also reported that the phenolic components are capable to inhibit some enzymes activity and the growth of microorganisms [88,89]. Lignin was introduced to the hydrogels as spherical CLPs due to the obvious advantages of their hydrophilic surface and dispersability in aqueous media.

The antioxidant activity (AA) of all the hydrogel scaffolds was evaluated by ABTS radical scavenging assay and expressed in milligrams of tannic acid equivalent (TAE) per gram of lignin as shown in Fig. 6a. The antioxidant activity of hydrogels was statistically similar showing that loading the hydrogel with gum did not influence the overall antioxidant activity. The gum did not present any radical scavenging

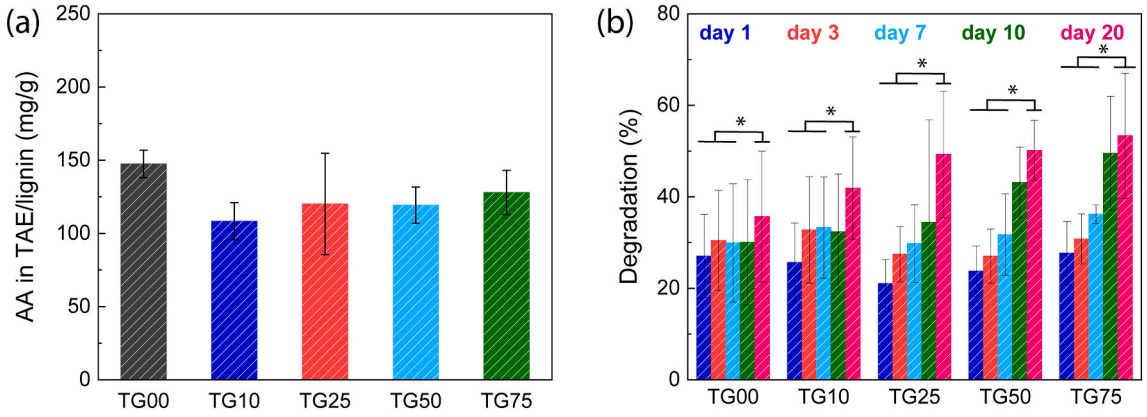

Fig. 6. (a) Antioxidant activity of dried scaffolds expressed in milligrams of tannic acid equivalent per gram of lignin. (b) Degradation study of the hydrogels in DBPS. Results expressed as mean ± SD, n = 3. *Compares brackets indicating significant values at the $p < 0.05$.

properties (0.05 ± 0.01 mg TAE g^{-1}) nor the TOCNF, hence only the lignin contributed to the antioxidant activity in the hydrogel. The AA was 147 ± 9 mg TAE g^{-1} lignin for control sample without gum (TG00) and decreased to 108–127 mg TAE g^{-1} for the other samples containing tragacanth gum. These results were superior to both CNF-CLP-alginate films (39 mg TAE g^{-1} lignin) and CLP dispersions (75 mg TAE g^{-1} lignin) reported previously [18]. Compared to CNF-CLP-alginate scaffolds and unmodified CNF, the TOCNF-CLPs-TG scaffolds prepared in this work are expected to have a higher internal porosity due to the stronger electrostatic repulsion between the hydrogel components, which enhances solvent diffusion and facilitates the access of $ABTS^{\bullet+}$ radical cations to the CLPs embedded in the scaffold. The slight decrease in mesoscale porosity, observed with tp-DSC upon increasing the TG content in the hydrogels (Fig. 2), did not affect this phenomenon indicating that the reswelling ability, which is enhanced by the TG addition is more important.

3.8. Scaffold degradation

The eventual degradation of the scaffolds is a common approach in some tissue engineering strategies, where the byproducts of the degraded scaffold must be non-toxic and able to leave the body without interfering with other organs. Since humans and animals do not have the enzyme cellulase, cellulose-based materials are in principle good candidates for implants where scaffold degradation is not required. Nevertheless, degradation tests can provide information about the stability of the scaffolds in physiological conditions. We evaluated the degradation of the hydrogel scaffolds in terms of loss of mass after incubation in DPBS solution at 37°C and 5 % carbon dioxide for several days. As can be seen in Fig. 6b, a more pronounced degradation was observed of the scaffolds with higher amount of TG, especially after 10 days. After 20 days the degradation rate was 0.4 %/day for TG00, 0.8 %/day for TG10, 1.4 %/day for TG25, 1.3 %/day for TG50 and 1.3 %/day for TG75. The decrease in mass can be explained by the detachment of the components loosely attached in the network during the washing with DI water, drying, and handling of the samples. High degradation rate could confirm the mild crosslinking of the components established by Ca^{+2} ions, leading to releasing the components which were not appropriately crosslinked. Hence the results suggest that TG favored degradation of the scaffolds. For a more complete or faster degradation, enzymes would be needed. For example, the abundant glycosidic linkages, such as a β-1-4 linked arabinogalactan and the linkages similar to pectin in TG can be cleaved by enzymatic action [90,91]. In previous reports, degradation studies were carried out with a matrix of degrading enzymes mimicking the *in vivo* process, where TG was incorporated in sodium alginate beads reaching almost 80 % degradation [91]. Other *in vitro* studies also reported complete degradation of TG inside gastrointestinal system [90].

3.9. Scaffold cytotoxicity test and cell proliferation

Hepatocellular carcinoma cell line (HepG2) was used as a model cell line to evaluate cytotoxicity and cell proliferation due to their high sensitivity to toxins [18,36]. Cells were seeded onto multicomponent scaffolds and also onto pure TOCNF. The WST-1 assay was used to determine the proliferation rate based on mitochondrial metabolic activity by colorimetric analysis. TOCNF based biomaterials have already been studied and present good biocompatibility, showing no signs of toxicological effect when cultured with myoblasts, fibroblasts, and liver cancer cells [21,92]. Fig. 7a displays the cell viability from WST-1 results after 1 day of incubation. Good cell viability (>90 %) was observed for all the samples, showing no signs of toxicity of the scaffolds to the cells. Compared to control samples (cells growing directly on a culture plate in 2D), the 3D hydrogel scaffolds presented greater cell viability. The 3D structure, swelling and porosity of the TG-containing scaffolds offered more surface available for cell seeding and facilitated the exchange of nutrients and cell waste between the cells and the environment [93]. Optical density of the hybrid hydrogels measured by colorimetric analysis at 420 nm presented significant differences in cellular metabolic activity after 1, 3, and 5 days of culture ($p < 0.05$) (Fig. 7b). High optical density values indicate increased metabolic activity due to production of the formazan product, which is directly correlated to cell viability and proliferation. All scaffold compositions presented high cell viability for all incubation periods meaning that the scaffolds were not toxic for the cells. Moreover, cell proliferation increased upon increasing TG content, which can be explained by the higher swelling ratio improving the surface area available for cell growth. In previous studies no cytotoxicity of TG against human fibroblast cells and human epithelial cells was reported [94,95]. This confirms the hydrogels provided a suitable environment and surface area for cell attachment, survival, and proliferation.

In order to better understand the spatial location of proliferated HepG2 cells inside the scaffolds, fluorescence microscopy was used. Cells were monitored over a 6-day period. The dense fibrillar network of the scaffolds severely limits optical light microscopy, as can be observed by the dark region of phase-contrast image, focused on the edge of the scaffold (Fig. S4). For this reason, Cell Proliferation Cytopainter (CP) and Propidium Iodide (PI) fluorescent dyes were used to qualitatively study the HepG2 cells within the scaffolds, in which green represents live cells, and red represents dead cells, respectively.

Live/dead double staining was performed in different scaffolds over a 6-day period (Fig. 8). The red fluorescent haze observed in some images is attributed to staining of the scaffold as well as dead cells in the dyeing process. Red fluorescent dots from PI related to dead cells was

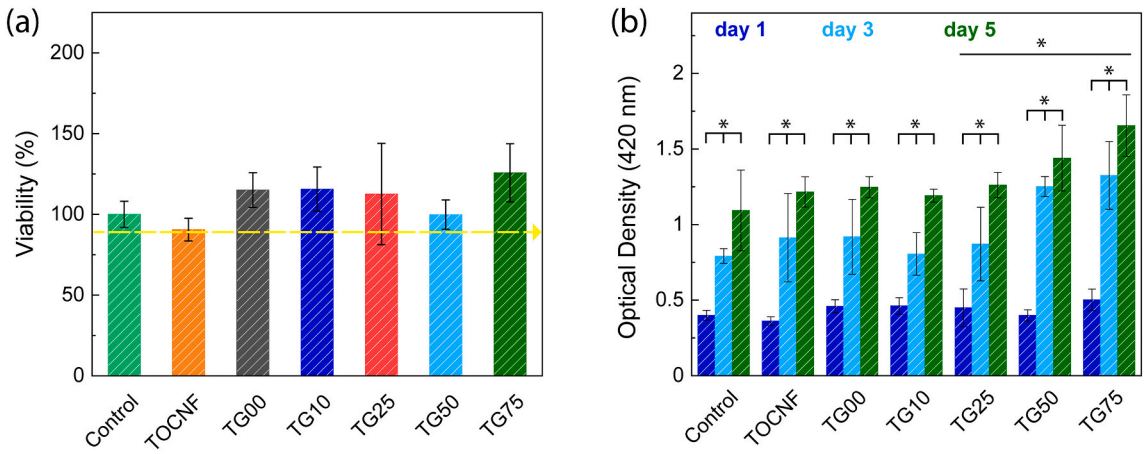

Fig. 7. (a) Cell viability of HepG2 cells in TOCNF and hydrogel scaffolds after day 1 of incubation; (b) optical density of HepG2 cells in the presence of different hydrogels after 1, 3 and 5 days assessed at 420 nm wavelength. Results expressed as mean ± SD, n = 3. *Indicating significant values at the $p < 0.05$. Vertical lines indicate that there is a significant difference between day 1, day 3 and day 5 for all samples and between samples TG25, TG50 and TG75.

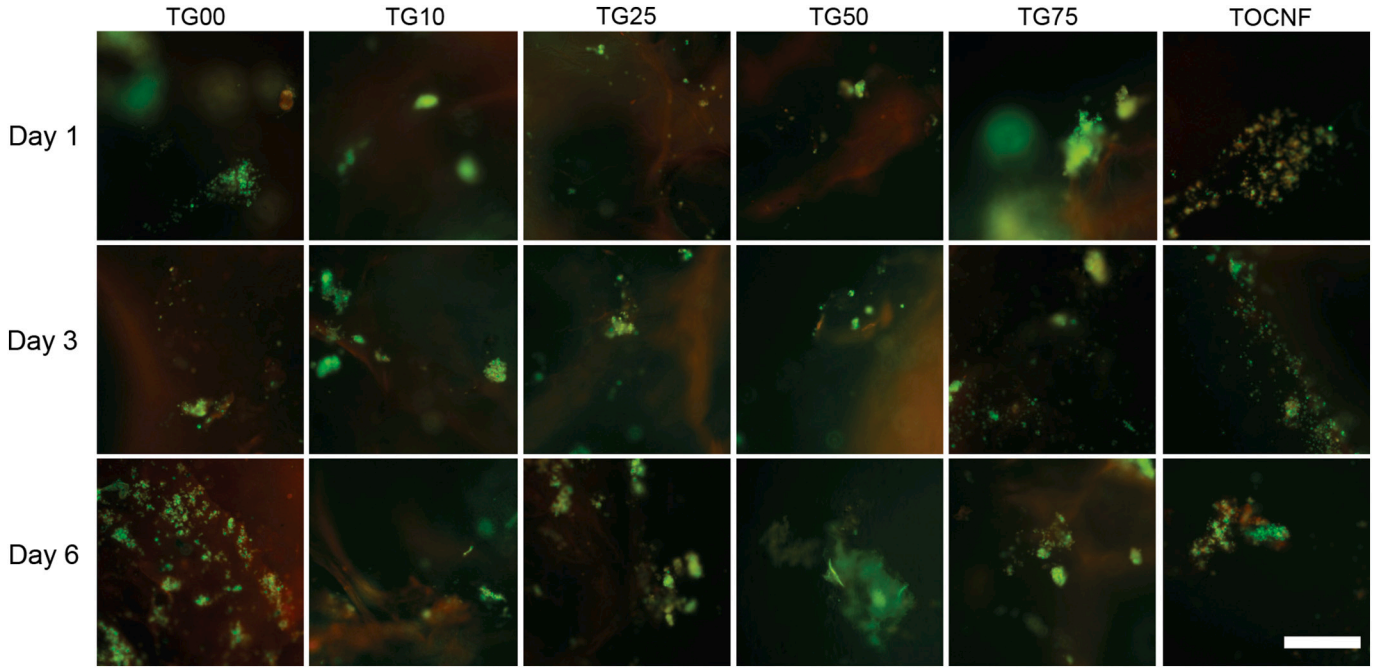

Fig. 8. Fluorescence microscopy images of HepG2 cells, seeded on the formulated scaffolds, confirm the viability of cells inside the scaffolds after 6 days. Merged PI/CP fluorescence images taken in five different TG concentrations (TG00, TG10, TG25, TG50, TG75) and pure TOCNF, monitored over a period of six days show the presence of viable cells in all conditions throughout the monitored incubation period. Scale bar 300 μm.

observed for all samples on day 1. This is because the cell handling process until seeding in the scaffolds causes physical stress to the cells leading to cell death as also observed previously [18]. Over time, the PI red signal faded away. The results revealed a high proportion of viable cells among all scaffolds investigated. Increasing TG concentrations didn't present negative effects on the viability and proliferation rates of cells inside the scaffolds, and clear clusters of cells can be observed at a wide variety of positions within the scaffold at different heights. Furthermore, the overall amount of HepG2 cells inside the TG scaffolds increased significantly from day 1 to day 3 and day 6, with an absence of dead cells. These observations support the findings displayed in Fig. 7b. Proliferation rate in the TG00 scaffold was noticeably lower than in the samples containing TG. The lowest proliferation rate was observed in the pure TOCNF scaffolds. Also, at each of the measurement points, cell clusters in this scaffold contained a high number of dead cells.

A 3D reconstruction of HepG2 cells inside TG75 scaffold was used to demonstrate the viability and proliferation after 6 days of culturing, deep within the scaffold (Fig. 9). We observed an abundance of cells present at different heights (Z-directions) up to 600 μm suggesting migration of cells to within the scaffold. This indicates that proliferation of cells occurs not only on the surfaces but also takes place inside the scaffolding structure. Altogether these results demonstrate excellent biocompatibility of the TOCNF-CLP-TG hydrogels as cell scaffolding materials and high potential in biomedical applications, where a tunable absorption rate and surface area are of great importance in cell culturing materials.

Moreover, tragacanth gum has been historically and widely used as an analgesic [8,96] in Iranian and Chinese medicine. Topical use has an analgesic action by inducing its antinociceptive effect by blocking α2-adrenoceptors in the adrenergic nervous system [9]. As already reported, topical application of TG in adult male rats resulted in completely closed wounds after 10 days, indicating that TG promoted

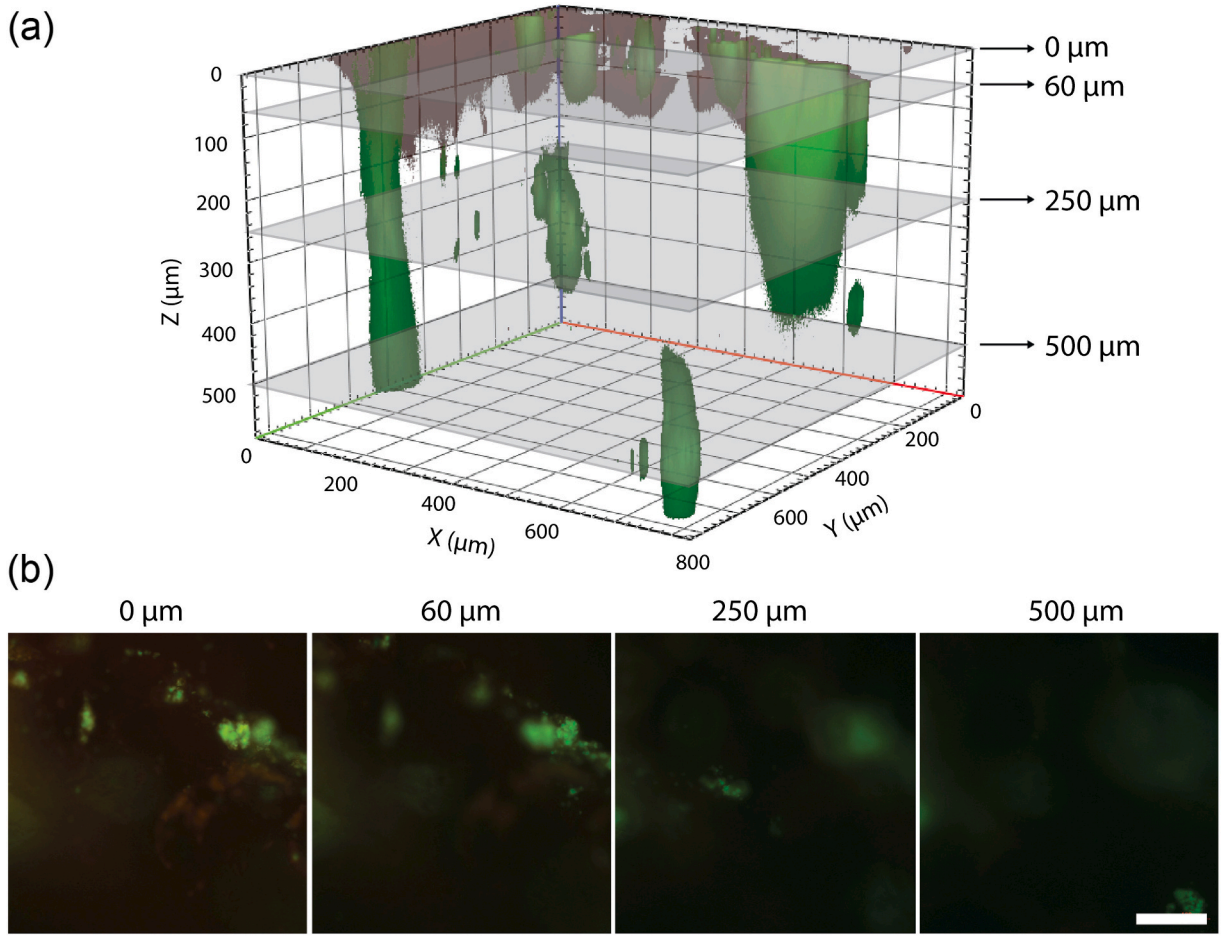

Fig. 9. (a) 3D reconstruction of Z-stacks acquired with 5 µm gaps from HepG2 cells grown in a TG75 scaffold after 6 days, confirms the presence of viable HepG2 cells at various vertical (Z) directions. (b) Merged PI/CP fluorescence images taken at 4 different vertical (Z) directions, displaying/focusing on viable cells at different heights. Images correspond to the gray box slices depicted in (a). Scale bar 300 µm.

wound contraction and healing [97] .

4. Conclusions

Undoubtedly, finding an ideal plant-based hydrogel that can mimic the properties of human tissue remains a challenge. A novel multicomponent hydrogel that was natural, sustainable, and biocompatible was developed using tragacanth gum combined with cellulose nanofibrils and lignin nanoparticles. The synergic effects of antioxidant activity of lignin, analgesic effect of tragacanth gum with the rheological properties of TOCNF make the hydrogel suitable for tissue engineering. The hydrogels presented shear-thinning behavior due to TOCNF along with tunable viscoelastic properties due to TG which enabled 3D printing of scaffolds with excellent printability. The scaffolds showed high swelling ratio and the degradation rate was enhanced by increasing TG content in the hydrogels. The evaluation of the mechanical properties revealed that the hydrogels are soft gels with stiffness at the level between skin and muscle tissues. The stiffness, viscosity and porosity of the hydrogels were furthermore easily controlled by changing the TG ratio enabling optimization for targeted applications. Cell viability tests demonstrated that the 3D-printed scaffolds were non-toxic and promoted proliferation of HepG2 cells. Due to all these properties, these plant-based multicomponent hydrogels are excellent candidates for designing soft materials for tissue engineering applications.

CRediT authorship contribution statement

Roberta Teixeira Polez: conceptualization, investigation, validation, methodology, formal analysis, visualization, writing – original draft.

Maria Morits: investigation, supervision, writing – review & editing.

Christopher Jonkergouw: investigation, visualization, writing – review & editing.

Josphat Phiri: investigation, supervision, writing – review & editing.

Juan José Valle-Delgado: supervision, writing – review & editing.

Markus B. Linder: resources, writing – review & editing.

Thaddeus Maloney: resources, writing – review & editing.

Orlando J. Rojas: supervision, resources, writing – review & editing, funding acquisition.

Monika Österberg: supervision, conceptualization, resources, writing – review & editing, project administration, funding acquisition.

Acknowlegments

This work was a part of the Academy of Finland's Flagship Program (project numbers 318890 and 318891, Competence Center for Materials Bioeconomy, FinnCERES). The authors would also like to thank Ms. Marja Kärkkäinen for providing TOCNF, Dr. Muhammad Farooq for providing TG, Dr. Leena Pitkänen for GPC analysis, and the Biohybrid Materials Research Group (Aalto University) for providing the HepG2 cells. This work made use of Aalto University Bioeconomy Facilities.

Appendix A. Supplementary data

Supplementary data to this article can be found online at https://doi.org/10.1016/j.ijbiomac.2022.06.153.

References

[1] A. Lewis, A. Koukoura, G.-I. Tsianos, A.A. Gargavanis, A.A. Nielsen, E. Vassiliadis, Organ donation in the US and Europe: the supply vs demand imbalance, Transplant. Rev. 35 (2021), 100585, https://doi.org/10.1016/j.trre.2020.100585.

[2] L. Bedian, A.M. Villalba-Rodríguez, G. Hernández-Vargas, R. Parra-Saldivar, H.M. N. Iqbal, Bio-based materials with novel characteristics for tissue engineering applications – a review, Int. J. Biol. Macromol. 98 (2017) 837–846, https://doi.org/10.1016/j.ijbiomac.2017.02.048.

[3] A.S. Moghaddam, H.A. Khonakdar, M. Arjmand, S.H. Jafari, Z. Bagher, Z. S. Moghaddam, M. Chimerad, M.M. Sisakht, S. Shojaei, Review of bioprinting in regenerative medicine: naturally derived bioinks and stem cells, ACS Appl. Bio Mater. 4 (2021) 4049–4070, https://doi.org/10.1021/acsabm.1c00219.

[4] A. Kirillova, T.R. Yeazel, D. Asheghali, S.R. Petersen, S. Dort, K. Gall, M.L. Becker, Fabrication of biomedical scaffolds using biodegradable polymers, Chem. Rev. 121 (2021) 11238–11304, https://doi.org/10.1021/acs.chemrev.0c01200, acs.chemrev.0c01200.

[5] P.A. Williams, G.O. Phillips, Handbook of Hydrocolloids, CRC Press, 2009, https://doi.org/10.1094/1891127381.toc.

[6] M. Nejatian, S. Abbasi, F. Azarikia, Gum tragacanth: structure, characteristics and applications in foods, Int. J. Biol. Macromol. 160 (2020) 846–860, https://doi.org/10.1016/j.ijbiomac.2020.05.214.

[7] C.A. Tischer, M. Iacomini, P.A.J. Gorin, Structure of the arabinogalactan from gum tragacanth (Astralagus gummifer), Carbohydr. Res. 337 (2002) 1647–1655, https://doi.org/10.1016/S0008-6215(02)00023-X.

[8] M.E. Taghavizadeh Yazdi, S. Nazarnezhad, S.H. Mousavi, M. Sadegh Amiri, M. Darroudi, F. Baino, S. Kargozar, Gum tragacanth (GT): a versatile biocompatible material beyond Borders, Molecules 26 (2021) 1510, https://doi.org/10.3390/molecules26061510.

[9] S.M. Bagheri, L. Keyhani, M. Heydari, M.H. Dashti-R, Antinociceptive activity of Astragalus gummifer gum (gum tragacanth) through the adrenergic system: a in vivo study in mice, J. Ayurveda Integr. Med. 6 (2015) 19, https://doi.org/10.4103/0975-9476.146543.

[10] E. Nazarzadeh Zare, P. Makvandi, F.R. Tay, Recent progress in the industrial and biomedical applications of tragacanth gum: a review, Carbohydr. Polym. 212 (2019) 450–467, https://doi.org/10.1016/j.carbpol.2019.02.076.

[11] C. Huang, H. Dong, Z. Zhang, H. Bian, Q. Yong, Procuring the nano-scale lignin in prehydrolyzate as ingredient to prepare cellulose nanofibril composite film with multiple functions, Cellulose 27 (2020) 9355–9370, https://doi.org/10.1007/s10570-020-03427-9.

[12] M. Farooq, T. Zou, G. Riviere, M.H. Sipponen, M. Österberg, Strong, ductile, and waterproof cellulose nanofibril composite films with colloidal lignin particles, Biomacromolecules 20 (2019) 693–704, https://doi.org/10.1021/acs.biomac.8b01364.

[13] E. Gerbin, G.N. Rivière, L. Foulon, Y.M. Frapart, B. Cottyn, M. Pernes, C. Marcuello, B. Godon, A. Gainvors-Claisse, D. Crônier, A. Majira, M. Österberg, B. Kurek, S. Baumberger, V. Aguié-Béghin, Tuning the functional properties of lignocellulosic films by controlling the molecular and supramolecular structure of lignin, Int. J. Biol. Macromol. 181 (2021) 136–149, https://doi.org/10.1016/j.ijbiomac.2021.03.081.

[14] M. Lievonen, J.J. Valle-Delgado, M.-L. Mattinen, E.-L. Hult, K. Lintinen, M. A. Kostiainen, A. Paananen, G.R. Szilvay, H. Setälä, M. Österberg, A simple process for lignin nanoparticle preparation, Green Chem. 18 (2016) 1416–1422, https://doi.org/10.1039/C5GC01436K.

[15] M. Österberg, M.H. Sipponen, B.D. Mattos, O.J. Rojas, Spherical lignin particles: a review on their sustainability and applications, Green Chem. 22 (2020) 2712–2733, https://doi.org/10.1039/D0GC00096E.

[16] P. Figueiredo, K. Lintinen, J.T. Hirvonen, M.A. Kostiainen, H.A. Santos, Properties and chemical modifications of lignin: towards lignin-based nanomaterials for biomedical applications, Prog. Mater. Sci. 93 (2018) 233–269, https://doi.org/10.1016/j.pmatsci.2017.12.001.

[17] M.H. Sipponen, H. Lange, C. Crestini, A. Henn, M. Österberg, Lignin for Nano- and Microscaled carrier systems: applications, trends, and challenges, ChemSusChem 12 (2019) 2039–2054, https://doi.org/10.1002/cssc.201900480.

[18] X. Zhang, M. Morits, C. Jonkergouw, A. Ora, J.J. Valle-Delgado, M. Farooq, R. Ajdary, S. Huan, M. Linder, O. Rojas, M.H. Sipponen, M. Österberg, Three-dimensional printed cell culture model based on spherical colloidal lignin particles and cellulose nanofibril-alginate hydrogel, Biomacromolecules 21 (2020) 1875–1885, https://doi.org/10.1021/acs.biomac.9b01745.

[19] M. Oprea, S.I. Voicu, Recent advances in composites based on cellulose derivatives for biomedical applications, Carbohydr. Polym. 247 (2020), 116683, https://doi.org/10.1016/j.carbpol.2020.116683.

[20] H. Seddiqi, E. Oliaei, H. Honarkar, J. Jin, L.C. Geonzon, R.G. Bacabac, J. Klein-Nulend, Cellulose and its derivatives: towards biomedical applications, Cellulose 28 (2021) 1893–1931, https://doi.org/10.1007/s10570-020-03674-w.

[21] R. Ajdary, S. Huan, N. Zanjanizadeh Ezazi, W. Xiang, R. Grande, H.A. Santos, O. J. Rojas, Acetylated nanocellulose for single-component bioinks and cell proliferation on 3D-printed scaffolds, Biomacromolecules 20 (2019) 2770–2778, https://doi.org/10.1021/acs.biomac.9b00527.

[22] M. Bhattacharya, M.M. Malinen, P. Lauren, Y. Lou, S.W. Kuisma, L. Kanninen, M. Lille, A. Corlu, C. Guguen-guillouzo, O. Ikkala, A. Laukkanen, A. Urtti, M. Yliperttula, Nanofibrillar cellulose hydrogel promotes three-dimensional liver cell culture, J. Control. Release 164 (2012) 291–298, https://doi.org/10.1016/j.jconrel.2012.06.039.

[23] Y.-R. Lou, L. Kanninen, T. Kuisma, J. Niklander, L.A. Noon, D. Burks, A. Urtti, M. Yliperttula, The use of nanofibrillar cellulose hydrogel as a flexible three-dimensional model to culture human pluripotent stem cells, Stem Cells Dev. 23 (2014) 380–392, https://doi.org/10.1089/scd.2013.0314.

[24] H. Baniasadi, R.T. Polez, E. Kimiaei, Z. Madani, O.J. Rojas, M. Österberg, J. Seppälä, 3D printing and properties of cellulose nanofibrils-reinforced quince seed mucilage bio-inks, Int. J. Biol. Macromol. 192 (2021) 1098–1107, https://doi.org/10.1016/j.ijbiomac.2021.10.078.

[25] J. Leppiniemi, Z. Mutahir, A. Dulebo, P. Mikkonen, M. Nuopponen, P. Turkki, V. P. Hytönen, Avidin-conjugated nanofibrillar cellulose hydrogel functionalized with biotinylated fibronectin and vitronectin promotes 3D culture of fibroblasts, Biomacromolecules 22 (2021) 4122–4137, https://doi.org/10.1021/acs.biomac.1c00579.

[26] M. Müller, E. Öztürk, Ø. Arlov, P. Gatenholm, M. Zenobi-Wong, Alginate sulfate-nanocellulose bioinks for cartilage bioprinting applications, Ann. Biomed. Eng. 45 (2017) 210–223, https://doi.org/10.1007/s10439-016-1704-5.

[27] E. Scarian, M. Bordoni, V. Fantini, E. Jacchetti, M.T. Raimondi, L. Diamanti, S. Carelli, C. Cereda, O. Pansarasa, Patients' stem cells differentiation in a 3D environment as a promising experimental tool for the study of amyotrophic lateral sclerosis, Int. J. Mol. Sci. 23 (2022) 5344, https://doi.org/10.3390/ijms23105344.

[28] M.H. Sipponen, M. Farooq, J. Koivisto, A. Pellis, J. Seitsonen, M. Österberg, Spatially confined lignin nanospheres for biocatalytic ester synthesis in aqueous media, Nat. Commun. 9 (2018) 2300, https://doi.org/10.1038/s41467-018-04715-6.

[29] A. Isogai, T. Saito, H. Fukuzumi, TEMPO-oxidized cellulose nanofibers, Nanoscale 3 (2011) 71–85, https://doi.org/10.1039/C0NR00583E.

[30] H. Fukuzumi, T. Saito, T. Iwata, Y. Kumamoto, A. Isogai, Transparent and high gas barrier films of cellulose nanofibers prepared by TEMPO-mediated oxidation, Biomacromolecules 10 (2009) 162–165, https://doi.org/10.1021/bm801065u.

[31] S. Fujisawa, Y. Okita, H. Fukuzumi, T. Saito, A. Isogai, Preparation and characterization of TEMPO-oxidized cellulose nanofibril films with free carboxyl groups, Carbohydr. Polym. 84 (2011) 579–583, https://doi.org/10.1016/j.carbpol.2010.12.029.

[32] T. Saito, A. Isogai, TEMPO-mediated oxidation of native cellulose. The effect of oxidation conditions on chemical and crystal structures of the water-insoluble fractions, Biomacromolecules 5 (2004) 1983–1989, https://doi.org/10.1021/bm0497769.

[33] M.A. Mohammadifar, S.M. Musavi, A. Kiumarsi, P.A. Williams, Solution properties of targacanthin (water-soluble part of gum tragacanth exudate from Astragalus gossypinus), Int. J. Biol. Macromol. 38 (2006) 31–39, https://doi.org/10.1016/j.ijbiomac.2005.12.015.

[34] M.H. Sipponen, M. Smyth, T. Leskinen, L.-S. Johansson, M. Österberg, All-lignin approach to prepare cationic colloidal lignin particles: stabilization of durable Pickering emulsions, Green Chem. 19 (2017) 5831–5840, https://doi.org/10.1039/C7GC02900D.

[35] V. Guccini, J. Phiri, J. Trifol, V. Rissanen, S.M. Mousavi, J. Vapaavuori, T. Tammelin, T. Maloney, E. Kontturi, Tuning the porosity, water interaction, and redispersion of nanocellulose hydrogels by osmotic dehydration, ACS Appl. Polym. Mater. 4 (2022) 24–28, https://doi.org/10.1021/acsapm.1c01430.

[36] V. Mersch-Sundermann, S. Knasmüller, X. Wu, F. Darroudi, F. Kassie, Use of a human-derived liver cell line for the detection of cytoprotective, antigenotoxic and cogenotoxic agents, Toxicology 198 (2004) 329–340, https://doi.org/10.1016/j.tox.2004.02.009.

[37] I. Slivac, E. Zdraveva, F. Ivančić, B. Žunar, T. Holjevac Grgurić, V. Gaurina Srček, I.-K. Svetec, T. Dolenec, E.G. Bajsić, M. Tominac Trcin, B. Mijović, Bioactivity comparison of electrospun PCL Mats and Liver extracellular matrix as scaffolds for HepG2 cells, Polymers (Basel) 13 (2021) 279, https://doi.org/10.3390/polym13020279.

[38] Int. Organ. Stand. ISO 10993-1, Biological Evaluation of Medical Devices - Part 1: Evaluation and Testing Within a Risk Management Process, Int. Organ. Stand., 2009.

[39] A. Schwab, R. Levato, M. D'Este, S. Piluso, D. Eglin, J. Malda, Printability and shape Fidelity of bioinks in 3D bioprinting, Chem. Rev. 120 (2020) 11028–11055, https://doi.org/10.1021/acs.chemrev.0c00084.

[40] A. Kurt, Physicochemical, rheological and structural characteristics of alcohol precipitated fraction of gum tragacanth, Food Heal. 4 (2018) 183–193, https://doi.org/10.3153/FH18019.

[41] H.A. Gavlighi, A.S. Meyer, D.N.A. Zaidel, M.A. Mohammadifar, J.D. Mikkelsen, Stabilization of emulsions by gum tragacanth (Astragalus spp.) correlates to the galacturonic acid content and methoxylation degree of the gum, Food Hydrocoll. 31 (2013) 5–14, https://doi.org/10.1016/j.foodhyd.2012.09.004.

[42] R. Aaen, S. Simon, F. Wernersson Brodin, K. Syverud, The potential of TEMPO-oxidized cellulose nanofibrils as rheology modifiers in food systems, Cellulose 26 (2019) 5483–5496, https://doi.org/10.1007/s10570-019-02448-3.

[43] J. Liao, K.A. Pham, V. Breedveld, TEMPO-CNF suspensions in the viscoelastic regime: capturing the effect of morphology and surface charge with a rheological parameter, Cellulose 28 (2021) 813–827, https://doi.org/10.1007/s10570-020-03572-1.

[44] L. Mendoza, W. Batchelor, R.F. Tabor, G. Garnier, Gelation mechanism of cellulose nanofibre gels: a colloids and interfacial perspective, J. Colloid Interface Sci. 509 (2018) 39–46, https://doi.org/10.1016/j.jcis.2017.08.101.

[45] A. Karppinen, T. Saarinen, J. Salmela, A. Laukkanen, M. Nuopponen, J. Seppälä, Flocculation of microfibrillated cellulose in shear flow, Cellulose 19 (2012) 1807–1819, https://doi.org/10.1007/s10570-012-9766-5.
[46] M. Iotti, Ø.W. Gregersen, S. Moe, M. Lenes, Rheological studies of microfibrillar cellulose water dispersions, J. Polym. Environ. 19 (2011) 137–145, https://doi.org/10.1007/s10924-010-0248-2.
[47] T. Yuan, J. Zeng, B. Wang, Z. Cheng, K. Chen, Lignin containing cellulose nanofibers (LCNFs): lignin content-morphology-rheology relationships, Carbohydr. Polym. 254 (2021), 117441, https://doi.org/10.1016/j.carbpol.2020.117441.
[48] M.I. Capitani, L.J. Corzo-Rios, L.A. Chel-Guerrero, D.A. Betancur-Ancona, S. M. Nolasco, M.C. Tomás, Rheological properties of aqueous dispersions of chia (Salvia hispanica L.) mucilage, J. Food Eng. 149 (2015) 70–77, https://doi.org/10.1016/j.jfoodeng.2014.09.043.
[49] B. Zhang, S.H. Chung, S. Barker, D. Craig, R.J. Narayan, J. Huang, Direct ink writing of polycaprolactone/polyethylene oxide based 3D constructs, Prog. Nat. Sci. Mater. Int. 31 (2021) 180–191, https://doi.org/10.1016/j.pnsc.2020.10.001.
[50] I. Zarzyka, M. Pyda, M.L. Di Lorenzo, Influence of crosslinker and ionic comonomer concentration on glass transition and demixing/mixing transition of copolymers poly(N-isopropylacrylamide) and poly(sodium acrylate) hydrogels, Colloid Polym. Sci. 292 (2014) 485–492, https://doi.org/10.1007/s00396-013-3092-9.
[51] A. Zerpa, L. Pakzad, P. Fatehi, Hardwood Kraft lignin-based hydrogels: production and performance, ACS Omega 3 (2018) 8233–8242, https://doi.org/10.1021/acsomega.8b01176.
[52] W.Y. Shih, W.-H. Shih, I.A. Aksay, Elastic and yield behavior of strongly flocculated colloids, J. Am. Ceram. Soc. 82 (2004) 616–624, https://doi.org/10.1111/j.1151-2916.1999.tb01809.x.
[53] J.L. Drury, D.J. Mooney, Hydrogels for tissue engineering: scaffold design variables and applications, Biomaterials 24 (2003) 4337–4351, https://doi.org/10.1016/S0142-9612(03)00340-5.
[54] J.N. Hay, P.R. Laity, Observations of water migration during thermoporometry studies of cellulose films, Polymer (Guildf). 41 (2000) 6171–6180, https://doi.org/10.1016/S0032-3861(99)00828-9.
[55] I.S. Raja, N.N. Fathima, Gelatin-cerium oxide nanocomposite for enhanced excisional wound healing, ACS Appl. Bio Mater. 1 (2018) 487–495, https://doi.org/10.1021/acsabm.8b00208.
[56] F. Cleymand, A. Poerio, A. Mamanov, K. Elkhoury, L. Ikhelf, J.P. Jehl, C.J.F. Kahn, M. Ponçot, E. Arab-Tehrany, J.F. Mano, Development of novel chitosan/guar gum inks for extrusion-based 3D bioprinting: process, printability and properties, Bioprinting. 21 (2021), e00122, https://doi.org/10.1016/j.bprint.2020.e00122.
[57] S. Zhu, L. Yao, C. Pan, J. Tian, L. Li, B. Luo, C. Zhou, L. Lu, 3D printed gellan gum/graphene oxide scaffold for tumor therapy and bone reconstruction, Compos. Sci. Technol. 208 (2021), 108763, https://doi.org/10.1016/j.compscitech.2021.108763.
[58] X. Zhang, Y. Yu, Z. Jiang, H. Wang, The effect of freezing speed and hydrogel concentration on the microstructure and compressive performance of bamboo-based cellulose aerogel, J. Wood Sci. 61 (2015) 595–601, https://doi.org/10.1007/s10086-015-1514-7.
[59] K.M. Rao, A. Kumar, K.S.V. Krishna Rao, A. Haider, S.S. Han, Biodegradable tragacanth gum based silver nanocomposite hydrogels and their antibacterial evaluation, J. Polym. Environ. 26 (2018) 778–788, https://doi.org/10.1007/s10924-017-0989-2.
[60] B. Singh, V. Sharma, Influence of polymer network parameters of tragacanth gum-based pH responsive hydrogels on drug delivery, Carbohydr. Polym. 101 (2014) 928–940, https://doi.org/10.1016/j.carbpol.2013.10.022.
[61] M.S. Hosseini, K. Hemmati, M. Ghaemy, Synthesis of nanohydrogels based on tragacanth gum biopolymer and investigation of swelling and drug delivery, Int. J. Biol. Macromol. 82 (2016) 806–815, https://doi.org/10.1016/j.ijbiomac.2015.09.067.
[62] J. Han, C. Zhou, Y. Wu, F. Liu, Q. Wu, Self-assembling behavior of cellulose nanoparticles during freeze-drying: effect of suspension concentration, particle size, crystal structure, and surface charge, Biomacromolecules 14 (2013) 1529–1540, https://doi.org/10.1021/bm4001734.
[63] W. Xu, B.Z. Molino, F. Cheng, P.J. Molino, Z. Yue, D. Su, X. Wang, S. Willför, C. Xu, G.G. Wallace, On low-concentration inks formulated by nanocellulose assisted with gelatin methacrylate (GelMA) for 3D printing toward wound healing application, ACS Appl. Mater. Interfaces 11 (2019) 8838–8848, https://doi.org/10.1021/acsami.8b21268.
[64] S. Nazarnezhada, G. Abbaszadeh-Goudarzi, H. Samadian, M. Khaksari, J. M. Ghatar, H. Khastar, N. Rezaei, S.R. Mousavi, S. Shirian, M. Salehi, Alginate hydrogel containing hydrogen sulfide as the functional wound dressing material: in vitro and in vivo study, Int. J. Biol. Macromol. 164 (2020) 3323–3331, https://doi.org/10.1016/j.ijbiomac.2020.08.233.
[65] X. Zhang, Y. Pan, S. Li, L. Xing, S. Du, G. Yuan, J. Li, T. Zhou, D. Xiong, H. Tan, Z. Ling, Y. Chen, X. Hu, X. Niu, Doubly crosslinked biodegradable hydrogels based on gellan gum and chitosan for drug delivery and wound dressing, Int. J. Biol. Macromol. 164 (2020) 2204–2214, https://doi.org/10.1016/j.ijbiomac.2020.08.093.
[66] Z. Rahmani, R. Sahraei, M. Ghaemy, Preparation of spherical porous hydrogel beads based on ion-crosslinked gum tragacanth and graphene oxide: study of drug delivery behavior, Carbohydr. Polym. 194 (2018) 34–42, https://doi.org/10.1016/j.carbpol.2018.04.022.
[67] A. Apoorva, A.P. Rameshbabu, S. Dasgupta, S. Dhara, M. Padmavati, Novel pH-sensitive alginate hydrogel delivery system reinforced with gum tragacanth for intestinal targeting of nutraceuticals, Int. J. Biol. Macromol. 147 (2020) 675–687, https://doi.org/10.1016/j.ijbiomac.2020.01.027.
[68] M.D. Torres, R. Moreira, F. Chenlo, M.J. Vázquez, Water adsorption isotherms of carboxymethyl cellulose, guar, locust bean, tragacanth and xanthan gums, Carbohydr. Polym. 89 (2012) 592–598, https://doi.org/10.1016/j.carbpol.2012.03.055.
[69] A. Kiani, H. Asempour, Hydrogel membranes based on gum tragacanth with tunable structures and properties. II. Comprehensive characterization of the swelling behavior, J. Appl. Polym. Sci. 126 (2012) E478–E485, https://doi.org/10.1002/app.36782.
[70] J. Qu, X. Zhao, Y. Liang, T. Zhang, P.X. Ma, B. Guo, Antibacterial adhesive injectable hydrogels with rapid self-healing, extensibility and compressibility as wound dressing for joints skin wound healing, Biomaterials 183 (2018) 185–199, https://doi.org/10.1016/j.biomaterials.2018.08.044.
[71] M.W. Tibbitt, K.S. Anseth, Hydrogels as extracellular matrix mimics for 3D cell culture, Biotechnol. Bioeng. 103 (2009) 655–663, https://doi.org/10.1002/bit.22361.
[72] A. Vedadghavami, F. Minooei, M.H. Mohammadi, S. Khetani, A. Rezaei Kolahchi, S. Mashayekhan, A. Sanati-Nezhad, Manufacturing of hydrogel biomaterials with controlled mechanical properties for tissue engineering applications, Acta Biomater. 62 (2017) 42–63, https://doi.org/10.1016/j.actbio.2017.07.028.
[73] K. Ghosh, Z. Pan, E. Guan, S. Ge, Y. Liu, T. Nakamura, X.-D. Ren, M. Rafailovich, R. A.F. Clark, Cell adaptation to a physiologically relevant ECM mimic with different viscoelastic properties, Biomaterials 28 (2007) 671–679, https://doi.org/10.1016/j.biomaterials.2006.09.038.
[74] H. Baniasadi, R. Ajdary, J. Trifol, O.J. Rojas, J. Seppälä, Direct ink writing of aloe vera/cellulose nanofibrils bio-hydrogels, Carbohydr. Polym. 266 (2021), 118114, https://doi.org/10.1016/j.carbpol.2021.118114.
[75] D. Zamani, F. Moztarzadeh, D. Bizari, Alginate-bioactive glass containing zn and mg composite scaffolds for bone tissue engineering, Int. J. Biol. Macromol. 137 (2019) 1256–1267, https://doi.org/10.1016/j.ijbiomac.2019.06.182.
[76] G.C. Reilly, A.J. Engler, Intrinsic extracellular matrix properties regulate stem cell differentiation, J. Biomech. 43 (2010) 55–62, https://doi.org/10.1016/j.jbiomech.2009.09.009.
[77] Y. Tang, S. Liu, Y. Deng, Y. Zhang, L. Yin, W. Zheng, An improved method for soft tissue modeling, Biomed. Signal Process. Control. 65 (2021), 102367, https://doi.org/10.1016/j.bspc.2020.102367.
[78] D. Klatt, U. Hamhaber, P. Asbach, J. Braun, I. Sack, Noninvasive assessment of the rheological behavior of human organs using multifrequency MR elastography: a study of brain and liver viscoelasticity, Phys. Med. Biol. 52 (2007) 7281–7294, https://doi.org/10.1088/0031-9155/52/24/006.
[79] Y. Zou, P.X. Liu, Q. Cheng, P. Lai, C. Li, A new deformation model of biological tissue for surgery simulation, IEEE Trans. Cybern. 47 (2017) 3494–3503, https://doi.org/10.1109/TCYB.2016.2560938.
[80] M.P. Ottensmeyer, J.K. Salisbury, In vivo data acquisition instrument for solid organ mechanical property measurement, in: W. Niessen, M.A. Viergever (Eds.), Med. Image Comput. Comput. Interv. – MICCAI 2001, Springer, Berlin, Heidelberg, 2001, pp. 975–982, https://doi.org/10.1007/3-540-45468-3_116.
[81] J. Visser, F.P.W. Melchels, J.E. Jeon, E.M. van Bussel, L.S. Kimpton, H.M. Byrne, W. J.A. Dhert, P.D. Dalton, D.W. Hutmacher, J. Malda, Reinforcement of hydrogels using three-dimensionally printed microfibres, Nat. Commun. 6 (2015) 6933, https://doi.org/10.1038/ncomms7933.
[82] M. Castilho, G. Hochleitner, W. Wilson, B. van Rietbergen, P.D. Dalton, J. Groll, J. Malda, K. Ito, Mechanical behavior of a soft hydrogel reinforced with three-dimensional printed microfibre scaffolds, Sci. Rep. 8 (2018) 1245, https://doi.org/10.1038/s41598-018-19502-y.
[83] M. Dizdaroglu, P. Jaruga, Mechanisms of free radical-induced damage to DNA, Free Radic. Res. 46 (2012) 382–419, https://doi.org/10.3109/10715762.2011.653969.
[84] R. Félix, P. Valentão, P.B. Andrade, C. Félix, S.C. Novais, M.F.L. Lemos, Evaluating the in vitro potential of natural extracts to protect lipids from oxidative damage, Antioxidants 9 (2020) 231, https://doi.org/10.3390/antiox9030231.
[85] Z. Li, J. Zhang, Y. Fu, L. Yang, F. Zhu, X. Liu, Z. Gu, Y. Li, Antioxidant shape amphiphiles for accelerated wound healing, J. Mater. Chem. B 8 (2020) 7018–7023, https://doi.org/10.1039/D0TB00578A.
[86] Z. Li, H. Li, J. Zhang, X. Liu, Z. Gu, Y. Li, Ultrasmall nanoparticle ROS scavengers based on polyhedral oligomeric silsesquioxanes, chinese, J. Polym. Sci. 38 (2020) 1149–1156, https://doi.org/10.1007/s10118-020-2486-7.
[87] S.R. Yearla, K. Padmasree, Preparation and characterisation of lignin nanoparticles: evaluation of their potential as antioxidants and UV protectants, J. Exp. Nanosci. 11 (2016) 289–302, https://doi.org/10.1080/17458080.2015.1055842.
[88] W. Yang, E. Fortunati, D. Gao, G.M. Balestra, G. Giovanale, X. He, L. Torre, J. M. Kenny, D. Puglia, Valorization of acid isolated high yield lignin nanoparticles as innovative Antioxidant/Antimicrobial organic materials, ACS Sustain. Chem. Eng. 6 (2018) 3502–3514, https://doi.org/10.1021/acssuschemeng.7b03782.
[89] L. Qin, W.-C. Li, L. Liu, J.-Q. Zhu, X. Li, B.-Z. Li, Y.-J. Yuan, Inhibition of lignin-derived phenolic compounds to cellulase, Biotechnol. Biofuels 9 (2016) 70, https://doi.org/10.1186/s13068-016-0485-2.
[90] H.A. Gavlighi, M. Michalak, A.S. Meyer, J.D. Mikkelsen, Enzymatic depolymerization of gum tragacanth: bifidogenic potential of low molecular weight oligosaccharides, J. Agric. Food Chem. 61 (2013) 1272–1278, https://doi.org/10.1021/jf304795f.
[91] S. Kulanthaivel, S.V.S. Rathnam, T. Agarwal, S. Pradhan, K. Pal, S. Giri, T.K. Maiti, I. Banerjee, Gum tragacanth–alginate beads as proangiogenic–osteogenic cell encapsulation systems for bone tissue engineering, J. Mater. Chem. B 5 (2017) 4177–4189, https://doi.org/10.1039/C7TB00390K.

[92] A. de Lima Pizi, N.F. Cândido, A.J.F. Fregonezi, E. Carvalho, F.A.Resende Trovatti, TEMPO-oxidized cellulose nanofibers in vitro cyto-genotoxicity studies, Bionanoscience 10 (2020) 766–772, https://doi.org/10.1007/s12668-020-00763-9.

[93] J. Liu, F. Cheng, H. Grénman, S. Spoljaric, J. Seppälä, J.E. Eriksson, S. Willför, C. Xu, Development of nanocellulose scaffolds with tunable structures to support 3D cell culture, Carbohydr. Polym. 148 (2016) 259–271, https://doi.org/10.1016/j.carbpol.2016.04.064.

[94] S. Ghayempour, M. Montazer, M. Mahmoudi Rad, Tragacanth gum biopolymer as reducing and stabilizing agent in biosonosynthesis of urchin-like ZnO nanorod arrays: a low cytotoxic photocatalyst with antibacterial and antifungal properties, Carbohydr. Polym. 136 (2016) 232–241, https://doi.org/10.1016/j.carbpol.2015.09.001.

[95] A. Fattahi, P. Petrini, F. Munarin, Y. Shokoohinia, M.A. Golozar, J. Varshosaz, M. C. Tanzi, Polysaccharides derived from tragacanth as biocompatible polymers and gels, J. Appl. Polym. Sci. 129 (2013) 2092–2102, https://doi.org/10.1002/app.38931.

[96] M.M. Zarshenas, A. Arabzadeh, M.A. Tafti, G. Kordafshari, A. Zargaran, A. Mohagheghzadeh, Application of herbal exudates in traditional Persian medicine, Galen Med. J. 1 (2012) 78–83.

[97] E. Fayazzadeh, S. Rahimpour, S.M. Ahmadi, S. Farzampour, M.S. Anvari, M. A. Boroumand, S.H. Ahmadi, Acceleration of skin wound healing with tragacanth (Astragalus) preparation: an experimental pilot study in rats, Acta Med Iran. 52 (2014) 3–8.